Accounting for uncertain fault geometry in earthquake source inversions – II: application to the Mw 6.2 Amatrice earthquake, central Italy

Théa Ragon, Anthony Sladen, Mark Simons

Geophysical Journal International

Geophys. J. Int. (2019) **218,** 689–707
Advance Access publication 2019 April 13
GJI Seismology

doi: 10.1093/gji/ggz180

Accounting for uncertain fault geometry in earthquake source inversions – II: application to the M_w 6.2 Amatrice earthquake, central Italy

Théa Ragon [1], Anthony Sladen[1] and Mark Simons[2]

[1] *Université Côte d'Azur, CNRS, Observatoire de la Côte d'Azur, IRD, Géoazur,* 250 *rue Albert Einstein,* 06560 *Valbonne, France. E-mail: ragon@geoazur.unice.fr*
[2] *Seismological Laboratory, California Institute of Technology,* 1200 *E. California Blvd., Pasadena, CA* 91125, *USA*

Accepted 2019 April 12. Received 2019 April 3; in original form 2018 November 22

SUMMARY

Our understanding of earthquake sources is limited by the availability and the quality of observations and the fidelity of our physical models. Uncertainties in our physical models will naturally bias our inferences of subsurface fault slip. These uncertainties will always persist to some level as we will never have a perfect knowledge of the Earth's interior. The choice of the forward physics is thus ambiguous, with the frequent need to fix the value of several parameters such as crustal properties or fault geometry. Here, we explore the impact of uncertainties related to the choice of both fault geometry and elastic structure, as applied to the 2016 M_w 6.2 Amatrice earthquake, central Italy. This event, well instrumented and characterized by a relatively simple fault morphology, allows us to explore the role of uncertainty in basic fault parameters, such as fault dip and position. We show that introducing uncertainties in fault geometry in a static inversion reduces the sensitivity of inferred models to different geometric assumptions. Accounting for uncertainties thus helps infer more realistic and robust slip models. We also show that uncertainties in fault geometry and Earth's elastic structure significantly impact estimated source models, particularly if near-fault observations are available.

Key words: Inverse theory; Probability distributions; Earthquake source observations.

1 INTRODUCTION

With scarce observations mainly limited to the surface of the Earth, our estimates of crustal properties and fault geometry are always uncertain. This imperfect knowledge is usually not accounted for in inferences of subsurface fault slip, with only observational errors considered. When imaging the slip on a fault, we often assume minimum complexity as a recognition of our inherent ignorance and to simplify the computation of the forward problem. For instance, we often assume the Earth is flat, that it can be approximated as a homogeneous elastic medium and that the causative fault geometry is simple and known. Uncertainties related to these approximations will affect the calculated response of the Earth and lead to different source models (e.g. Simons *et al.* 2002; Beresnev 2003; Hartzell *et al.* 2007; Dettmer *et al.* 2014; Diao *et al.* 2016; Ragon *et al.* 2018). These so-called epistemic uncertainties can be many orders of magnitude greater than observational uncertainties for large earthquakes (Ragon *et al.* 2018). In this study, we investigate uncertainties related to our poor knowledge of the geometry of the causative fault and elastic structure.

Fault geometry for a given earthquake is generally deduced from a variety of observations including surface rupture, centroid moment tensor solutions, previous earthquakes, aftershocks distributions or tomography. Because of observational inaccuracies or simply a lack of data, it is usual to describe the causative fault by a reduced set of fixed parameters (location, strike, dip, length, width) to define one or several planar, or at least smoothly varying, fault segments. Yet, we know from field investigations and modelling that seismogenic faults are complex systems, at least at the surface (e.g. Segall & Pollard 1980; Okubo & Aki 1987; Peacock 1991; Walsh *et al.* 2003; Manighetti *et al.* 2015). At depth, fault complexity is still an open question (Graymer *et al.* 2007; Wei *et al.* 2011; Ross *et al.* 2017). Though, faults are thought to be non-planar at all scales (e.g. Power *et al.* 1987; Candela *et al.* 2012). The variability of proposed fault morphology for many events, such as the 2009 M_w 6.3 L'Aquila (Lavecchia *et al.* 2012), the October 2016 Norcia (Bonini *et al.* 2019), the 2011 M_w 9.0 Tohoku–Oki (e.g. Lay 2018), the 1999 M_w 7.4 Izmit (e.g. Duputel *et al.* 2014) or the 2015 M_w 7.8 Gorkha events (e.g. Wang & Fialko 2015; Elliott *et al.* 2016; Yue *et al.* 2017), suggests that even with a large amount of observations and prior seismotectonic knowledge of the area, it is not possible

to robustly determine fault geometry, and neither to choose the most realistic architecture. In the following, we only address uncertainties in basic fault geometry parameters, such as fault dip and position, and the fault we assume for inversion (planar, not rough) thus remains different than the structures we observe (complex and rough).

To address our uncertain assumptions on the causative fault geometry, we previously proposed a practical framework based on a sensitivity analysis (Ragon *et al.* 2018, hereafter referred to as RSS18). There we described a methodology to account for uncertainties of the fault geometry parameters, such as fault dip, position, strike or curvature, following the framework described in Duputel *et al.* (2014). This methodology has been validated through a toy model, but it remains to be explored in the case of a real earthquake. The impact of uncertainties in fault geometry is particularly striking for a simple 2-D case (as in RSS18). Yet, for a real event, the information brought by laterally extensive observations could potentially minimize the influence of epistemic uncertainties. Here, as with the toy model study, we focus on the effect of fault dip and position as they cover two primary sources of fault geometry uncertainties. To analyse and illustrate the impact of these first-order parameters independently of other geometric characteristics (curvature, variation in strike,...), we consider an earthquake that ruptured a relatively simple fault geometry, the M_w 6.2 earthquake that struck central Italy in August 2016. This event is characterized by a clear surface rupture and a well-observed causative fault geometry (EMERGEO Working Group 2016a; Cheloni *et al.* 2017; Pucci *et al.* 2017). The choice of the Amatrice event is also motivated by the large density of available near-field observations, the good coverage of geodetic data and the overall quality of the instrumentation. The availability of near-field data is important since RSS18 showed that far-field observations are less sensitive to a change in fault geometry, and tend to induce less bias in the inferred source model. As an intermediate magnitude earthquake, epistemic uncertainties will not be as influential as they could be for a large event (e.g. $M_w \geq 8$). But the observational errors are limited, allowing us to emphasize the effect of epistemic uncertainties.

We begin by quantifying the uncertainties in the fault geometry (for fault dip and position) and in crustal structure for the 2016 M_w 6.2 Amatrice earthquake, using available observations and published studies. We then compare co-seismic slip models inferred assuming different fault geometries. Accounting for uncertainties in both fault dip and position, we explore the influence of uncertainties in the fault geometry in the distribution of co-seismic subsurface fault slip. Finally, we describe our preferred model, as constrained by geodetic data, for the August 2016 earthquake.

2 THE 2016 AUGUST 24 M_w 6.2 EARTHQUAKE

2.1 The 2016 seismic sequence of central Italy

The M_w 6.2 2016 August 24 earthquake was the first of a series of moderate to large events, with five events of more than M_w 5.0, all of which activated a normal fault system located in the central Apennines. In the following, we refer to the 2016 August 24 event as the Amatrice earthquake. On October 26th and 30th, 2 months after the onset of the Amatrice sequence, M_w 5.9 and M_w 6.5 earthquakes occurred a few tenth of kilometres to the north, near the town of Norcia (Fig. 1). Overall, this sequence mainly ruptured the Mt Bove-Mt Vettore-Mt Gorzano fault system, as evidenced by co-seismic surface ruptures (EMERGEO Working Group 2016a,b; Pucci *et al.* 2017). The Amatrice event ruptured to the surface over more than 5 km along the southern part of the Mt Vettore fault, with an estimated maximal vertical offset of 30 cm (Fig. 1; EMERGEO Working Group 2016a; Pucci *et al.* 2017). The ruptured geometry of the Amatrice event appears to be a lot simpler than for the October 2016 shocks, which may have ruptured several fault segments and antithetic faults (EMERGEO Working Group 2016b; Cheloni *et al.* 2017; Chiaraluce *et al.* 2017).

2.2 Geometry of the causative fault

Numerous observations are available to constrain the fault geometry of the Amatrice earthquake, including ground surface deformation derived from surface rupture (Fig. 1) and satellite imagery, distribution of aftershocks and aftershocks focal mechanisms. The continuous part of the surface rupture delineates a curved path with an average strike of 155° (e.g. EMERGEO Working Group 2016a; Pucci *et al.* 2017), consistent with the strike of seismogenic faults identified from previous earthquakes and geological data (Fig. 1, e.g. Boncio *et al.* 2004b). The fault geometry is constrained at depth by the distribution of relocated aftershocks that occurred after the 24 August event (e.g. Bonini *et al.* 2016; Michele *et al.* 2016; Chiaraluce *et al.* 2017). Vertical sections orthogonally oriented to the fault trend show that the causative fault can be well described by a main segment dipping 35–40° (Bonini *et al.* 2016; Cheloni *et al.* 2017). However, the aftershock cluster is too scattered to determine a clear fault geometry, and possible structures could dip from 30° to 55° with an uncertainty on fault surface trace location of more than 5 km.

This uncertainty in fault geometry is also in published focal mechanisms or fault geometries. Dip and strike parameters of available focal mechanisms vary by more than 12° and 30°, respectively (Liu *et al.* 2017). Most published analyses of the Amatrice earthquake agree on modelling the causative fault as one main segment. But assumed fault parameters differ significantly from one model to another. Strike and fault position have generally been determined from nodal planes and/or interferometric synthetic aperture radar (InSAR) frames (Tinti *et al.* 2016; Huang *et al.* 2017b; Liu *et al.* 2017), giving strike values ranging from N155° (Liu *et al.* 2017) to N167° (Huang *et al.* 2017b). When the fault strike is inverted from GPS or InSAR data, inferred value is around N161° (respectively, Cheloni *et al.* 2016; Lavecchia *et al.* 2016). The fault dip is also generally solved for, and inferred dip values range between 34° and 51° (Bonini *et al.* 2016; Cheloni *et al.* 2016; Lavecchia *et al.* 2016; Tinti *et al.* 2016; Huang *et al.* 2017b; Liu *et al.* 2017; Pizzi *et al.* 2017; Tung & Masterlark 2018). Fault position and length are also highly variable, resulting in up to 3 km offset between published fault traces. Tung & Masterlark (2018) also show that the variability of solved fault geometry parameters is highly influenced by the assumed earth model.

Fault morphologies used for the Amatrice event are, as for the 2009 M_w 6.3 L'Aquila (Lavecchia *et al.* 2012) or the M_w 9.0, 2011, Tohoku–Oki events (Lay 2018), extremely variable. For the Amatrice earthquake, uncertainty of dip and strike parameters reaches 10–15°, and uncertainty of fault surface position is of 2–5 km (Fig. 1).

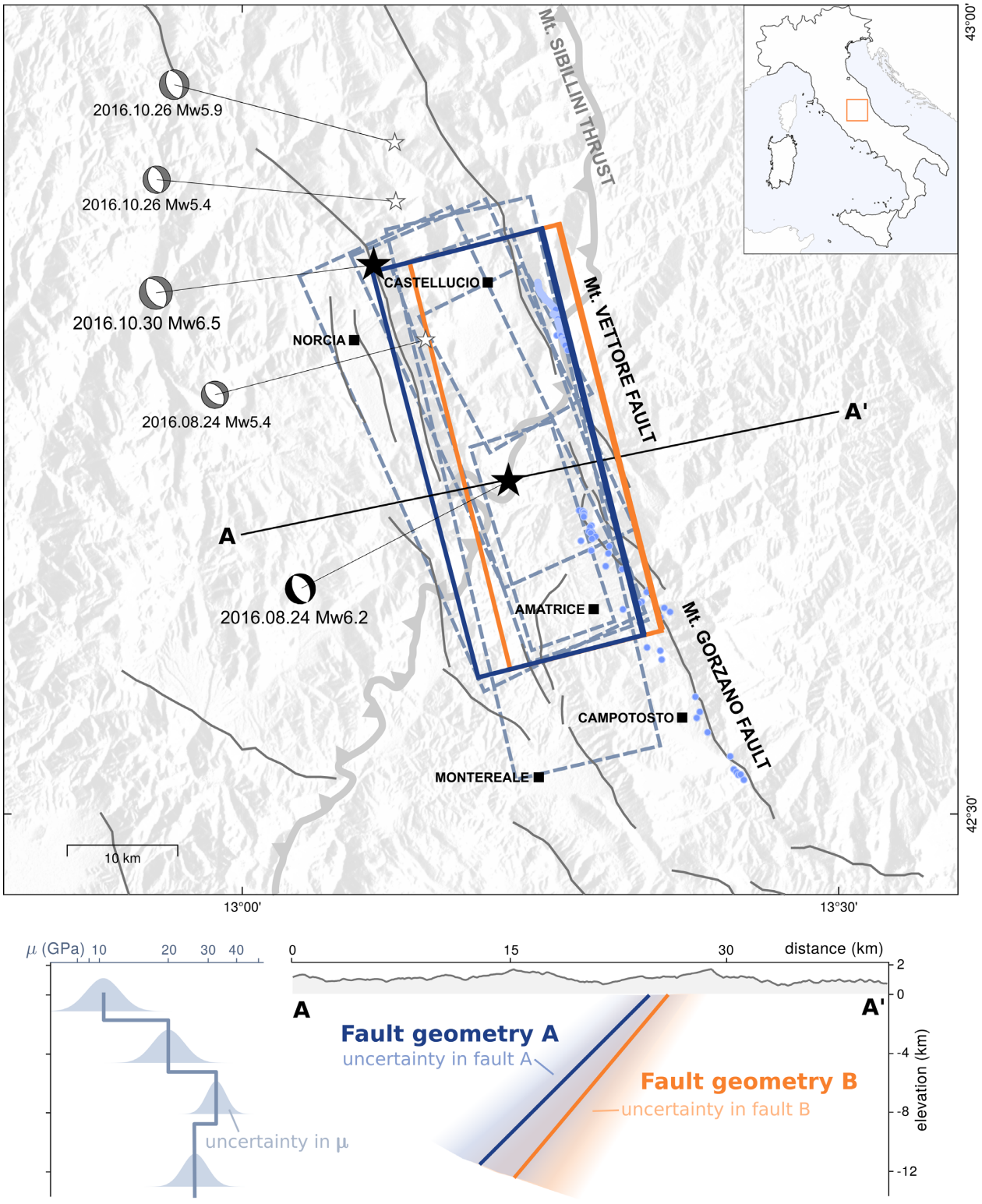

Figure 1. Seismotectonic framework of the area involved in the 2016 seismic sequence (top), and assumed forward model and associated uncertainties (bottom). In the map (top), the solid grey lines are the major seismogenic faults of the area (Boncio *et al.* 2004a), while assumed causative faults for the published finite-fault studies (Lavecchia *et al.* 2016; Tinti *et al.* 2016; Cheloni *et al.* 2017; Chiaraluce *et al.* 2017; Huang *et al.* 2017b; Liu *et al.* 2017) are shown as the dashed grey lines. Identified surface rupture areas of the August 24 earthquake are plotted with the blue dots (Pucci *et al.* 2017). Beach balls are the focal mechanisms of the two mainshocks and three main aftershocks (moment tensor solutions from the INGV Time Domain Moment Tensor catalog available at http://cnt.rm.ingv.it/en/tdmt), with their respective epicentres located by the black and white stars. Our preferred fault geometry (fault geometry A) is delineated with the dark blue line, while the fault geometry B is in orange. This colours are the same for the elevation profile (bottom), where uncertainties in each fault geometry are also represented. The assumed elastic modulus μ and associated uncertainties are also illustrated for the 12 first kilometres below the Earth surface. For a more complete view of assumed crustal properties, refer to Supporting Information Fig. S1.

2.3 Crustal structure

Duputel *et al.* (2014) showed how to account for uncertain elastic structure. RSS18 showed that accounting for uncertainties in both fault geometry and crustal structure is necessary to infer reliable slip models for a simplified toy model. Here, we will also estimate the impact of uncertainties in the crustal model in order to evaluate the relative influence of each type of uncertainty.

The crustal structure of central Italy is well studied. Numerous 1-D velocity models have been published, inverted from background seismicity (Bagh *et al.* 2007), from receiver functions (Bianchi *et al.* 2010) or surface waves (Herrmann *et al.* 2011; Ameri *et al.* 2012). Yet, these earth models are subject to inaccuracies, with standard deviation for V_s reaching more than 90 per cent at the surface and reaching up to 30 per cent below 10 km depth, when the deviation is calculated (Bianchi *et al.* 2010). Moreover, 1-D V_s models can also differ by more than 1 km s^{-1} (Herrmann *et al.* 2011). This discrepancy can be due to observational errors, data processing errors, inversion bias and also the effect of 3-D structure. The mass density is also needed to constrain elastic rigidity. Yet, published density models also vary up to 14 per cent in the first kilometres below the Earth surface, the discrepancies between models decreasing to ∼5 per cent at depths greater than 20 km (Herrmann *et al.* 2011; Magnoni *et al.* 2014).

The lateral variability of 3-D models describing the crust of central Italy, at a large scale (e.g. Chiarabba *et al.* 2010; Magnoni *et al.* 2014) or around the L'Aquila event area (Di Stefano *et al.* 2011), can help infer the uncertainty of 1-D profiles when used to analyse an extended area. For V_p, the lateral variability below 5 km depth reaches the maximum value of 0.6 km s^{-1} for the small-scale model (Di Stefano *et al.* 2011) and 1.5 km s^{-1} for the central Italy model (Chiarabba *et al.* 2010). Between 5 and 15 km depth, V_p can vary by more than 1.5 km s^{-1} laterally, and below 15 km depth the lateral variability decreases to less than 0.5 km s^{-1} (Chiarabba *et al.* 2010; Magnoni *et al.* 2014). Thus, at depths shallower than 15 km, layered models have V_p ranging from 4.7 to 6 km s^{-1}, reflecting up to 25-31 per cent of variability according to 3-D models. And deeper than 15km, V_p is 7 km s^{-1} on average with a lateral variability of 8 per cent.

The influence of 3-D crustal structure on source estimation problems (even for geodetic problems) was illustrated on the 2009 L'Aquila earthquake, which occurred 50 km south of the Amatrice event (e.g. Trasatti *et al.* 2011; Gallovic *et al.* 2015). Accounting for uncertainties in elastic properties of our assumed earth model, regardless of the complexity of the model, may thus be particularly important also for the Amatrice earthquake. Based on the lateral variability of 3-D crustal models and the heterogeneity of density models, the shear modulus of the Amatrice area may vary by 2–8 per cent at depths greater than 15 km and up to 20 per cent at shallower depths (Fig. 1 and Supporting Information Fig. S1).

3 INVERSION FRAMEWORK

3.1 Data

We use GPS offsets from 46 stations and 4 InSAR frames. We use the co-seismic GPS offsets and errors provided by INGV (GPS data and data analysis center 2016). The co-seismic measurements were estimated based on 3 d of continuous GPS stations position before and after the main shock. We include GPS observations taken within 80 km in the north–south direction of the epicentre, the displacement at farther stations do not add more useful information to the inverse problem. Data errors are used to build a diagonal covariance matrix describing observational uncertainties.

We use two ALOS-2 InSAR frames and two Sentinel frames. The ALOS-2 images have been acquired by the Japan Aerospace Exploration Agency and processed by Huang *et al.* (2017b). The Sentinel-1 images have been acquired under the Copernicus program by the European Space Agency. The Sentinel-1 interferograms have been processed using the TopsApp module of the InSAR Scientific Computing Environment (ISCE) software within the ARIA project (NASA/JPL-Caltech). The co-seismic interferograms are distributed in two ascending and two descending frames (more information can be found in Supporting Information Table S1). For computational efficiency, we resample InSAR observations based on model resolution (Lohman & Simons 2005). To build a data covariance matrix for the InSAR data, we mask the area of co-seismic displacement and estimate empirical covariograms as a function of distance between data points (Supporting Information Fig. S2). The InSAR covariance matrix is calculated from the best-fitting exponential function to empirical covariograms (Jolivet *et al.* 2012), and merged with the diagonal GPS covariance matrix to form the full data covariance matrix $\mathbf{C}_d$.

3.2 Forward model

As the causative fault is probably not multisegmented (Lavecchia *et al.* 2016; Tung & Masterlark 2018) and for the sake of simplicity, we assume a simple planar fault geometry. We determine strike and position from surface rupture observations (Pucci *et al.* 2017), surface deformation observed in the interferograms and formerly identified seismogenic faults (e.g. Boncio *et al.* 2004b). We select dip and width from aftershocks locations and focal mechanisms (e.g. Chiaraluce *et al.* 2017). Our preferred fault plane extends over 28 km south of coordinates (13.2508°E, 42.8575°N) with a strike of N166°. We set fault dip at 45° and width at 16 km, such that the fault is reaching the ground surface. This geometry is in agreement with already proposed causative structures (see Section 2.2). For the purpose of slip imagery, the fault is divided into 240 square subfaults of 1.3 km side.

We perform the geodetic inversions assuming a 1-D layered elastic structure based on the CIA model (Herrmann *et al.* 2011), and calculate Green's functions with the EDKS software (derived from Zhu & Rivera 2002).

3.3 Accounting for epistemic uncertainties

When one assumes a set of forward parameters, Ψ_{prior} (e.g. fault geometry and elastic parameters), which are the most realistic *a priori*, we implicitly include epistemic uncertainties in our inverse problem. These uncertainties of the forward model reflect our imperfect knowledge of the predictions $\mathbf{d}_{\text{pred}} = \mathbf{G}(\Psi_{\text{prior}}) \cdot \mathbf{m}$ for an inferred source model $\mathbf{m}$ and the assumed set of non-inverted parameters Ψ_{prior}.

If we assume that the errors on surface displacement $\mathbf{d}$ follow a Gaussian distribution centred on the predictions $\mathbf{d}_{\text{pred}}$ with a prediction covariance matrix $\mathbf{C}_p(\mathbf{m})$, then the discrepancies between observations $\mathbf{d}_{\text{obs}}$ and forward predictions $\mathbf{d}_{\text{pred}} = \mathbf{G}(\Psi_{\text{prior}}) \cdot \mathbf{m}$ can be quantified by a misfit function of the form

$$\chi(\mathbf{m}) = \frac{1}{2}[\mathbf{d}_{\text{obs}} - \mathbf{G}(\Psi_{\text{prior}}) \cdot \mathbf{m}]^T \times \mathbf{C}_\chi^{-1} \cdot [\mathbf{d}_{\text{obs}} - \mathbf{G}(\Psi_{\text{prior}}) \cdot \mathbf{m}], \quad (1)$$

where $\mathbf{C}_\chi(\mathbf{m})$ is the misfit covariance matrix (Tarantola 2005; Minson *et al.* 2013, 2014; Duputel *et al.* 2014) and is defined as

$$\mathbf{C}_\chi(\mathbf{m}) = \mathbf{C}_\mathrm{d} + \mathbf{C}_\mathrm{p}(\mathbf{m}), \tag{2}$$

where $\mathbf{C}_\mathrm{d}$ is the covariance matrix of the observations and $\mathbf{C}_\mathrm{p}$ the covariance matrix of the predictions.

As developed in Duputel *et al.* (2014) for the elastic properties and RSS18 for the fault geometry, the linearized prediction covariance matrix can be expressed as

$$\mathbf{C}_\mathrm{p} = \mathbf{K}_\Psi \cdot \mathbf{C}_\Psi \cdot \mathbf{K}_\Psi^T, \tag{3}$$

where $\mathbf{C}_\Psi$ is a diagonal matrix describing the standard deviation of the *a priori* distribution of parameters Ψ. $\mathbf{K}_\Psi$ is the sensitivity kernel of the predictions with respect to fault geometry parameters, such that

$$(\mathbf{K}_\Psi^G)_{ij}(\Psi_\mathrm{prior}) = \frac{\partial\, G_{ij}}{\partial\, \Psi}(\Psi_\mathrm{prior}), \tag{4}$$

$$\mathbf{K}_\Psi = \mathbf{K}_\Psi^G \cdot \mathbf{m}_\mathrm{prior}, \tag{5}$$

with $\mathbf{G}$ being the matrix of Green's functions and $\mathbf{m}_\mathrm{prior}$ an *a priori* assumed source model. We can then pre-compute the sensitivity kernels $\mathbf{K}_\Psi^G$ without any dependence on the assumed model $\mathbf{m}_\mathrm{prior}$. In this study, we account for uncertainties in fault geometry as discussed in RSS18, as well as in the Earth elastic properties (as in Duputel *et al.* 2014). We can express the full uncertainty covariance matrix as the sum of the different uncertainty terms: $\mathbf{C}_\chi = \mathbf{C}_\mathrm{d} + \mathbf{C}_\mathrm{p}^\mathrm{fault} + \mathbf{C}_\mathrm{p}^\mathrm{earth}$.

3.3.1 *Uncertainty in fault geometry*

We concentrate here on the impact of fault dip and position, as in RSS18, a parametrization motivated by simplicity and the large range of probable fault configurations that can then be addressed. We calculate $\mathbf{C}_\mathrm{p}^\mathrm{fault}$ following eq. (3) with Ψ corresponding to either fault dip or fault tip position. First, we pre-compute the sensitivity kernels $\mathbf{K}_\mathrm{dip}$ and $\mathbf{K}_\mathrm{shift}$ following eq. (4). Considering an incorrect dip or shift of the fault Ψ_prior and a range of uncertainty e, we compute the Green's functions matrices $\mathbf{G}_{\Psi_\mathrm{i}}$ for each fault parameter in the range $[\Psi_\mathrm{prior} - e; \Psi_\mathrm{prior} + e]$. Each element of $\mathbf{K}_\mathrm{shift}$ or $\mathbf{K}_\mathrm{dip}$ is estimated by the slope of the linear regression of $\mathbf{G}_\Psi$. Our *a priori* chosen dip is of 45° with a 0 km fault shift. We assume a range of uncertainty (e) of 10° for the fault dip, and 2 km for the fault surface position. As initial model $\mathbf{m}_\mathrm{prior}$, we choose a uniform slip model derived from the centroid moment tensor solution.

The choice of the standard deviation of *a priori* chosen parameters (dip or position) is motivated by the results of our literature review as discussed above in Section 2.2. Aftershocks distribution and published fault models agree on the fault dip with approximately 10° of uncertainty. We thus choose a covariance $\mathbf{C}_\mathrm{dip}$ corresponding to a standard deviation of 5° from the assumed value (45° in our case). Uncertainty on fault position can range from 2 to 5 km in the strike perpendicular direction, so we assume a standard deviation for $\mathbf{C}_\mathrm{shift}$ of 2 km. We can then express uncertainty in fault geometry as $\mathbf{C}_\mathrm{p}^\mathrm{fault} = \mathbf{C}_\mathrm{p}^\mathrm{dip} + \mathbf{C}_\mathrm{p}^\mathrm{shift}$.

3.3.2 *Uncertainty in Earth structure*

In practice, we consider that $\Psi_\mathrm{prior} = \ln \Omega$ for given elastic parameters Ω, as used in Duputel *et al.* (2014). In this case, the distribution of elastic parameters is log-normal. Our prior elastic model has eight layers of varying properties (Herrmann *et al.* 2011), we thus pre-compute eight different kernels to estimate the influence of each layer on Green's functions. We choose the standard deviation for each layer based on the lateral variability of 3-D crustal models and the heterogeneity of density models, as previously detailed in Section 2.3, resulting in conservative standard deviations on the logarithm of the shear modulus of 0.08 at depths greater than 15 km and 0.44 at shallower depths (the mean of $\ln \mu$ varying between 2.5 and 4, with μ in GPa).

3.4 Bayesian sampling approach

Instead of trying to infer the best solution of the inverse problem, we choose to sample the solution space and image its probable models. We solve our problem with a Bayesian sampling approach allowing us to infer the posterior uncertainty of inferred models. This approach relies on the AlTar package, a reformulation of the code CATMIP (Minson *et al.* 2013). AlTar combines the Metropolis algorithm with a tempering process to realize an iterative sampling of the solution space of the source models. A large number of samples are tested in parallel at each transitional step. Additionally, an important resampling step is performed at the end of each tempering step. The probability of each sample to be selected depend on its capacity to fit the observations $\mathbf{d}_\mathrm{obs}$ within the uncertainties $\mathbf{C}_\chi$.

The ability of each model parameter to solve the source problem is evaluated through repeated updates of the probability density functions (PDFs):

$$f(\mathbf{m}, \beta_i) \propto p(\mathbf{m}) \cdot \exp[-\beta_i \cdot \chi(\mathbf{m})], \tag{6}$$

with $\mathbf{m}$ being the current sample and $p(\mathbf{m})$ the prior information on this sample, $\chi(\mathbf{m})$ being the misfit function, i corresponding to each iteration and β evolving dynamically from 0 to 1 to improve the efficiency of the parameter space exploration (Minson *et al.* 2013).

We specify prior distributions for each model parameter. We use a zero-mean Gaussian prior $p(\mathbf{m}) = \mathcal{N}(0\,\mathrm{cm}, 10\,\mathrm{cm})$ on the strike-slip component as we assume that most of the slip is occurring in the down-dip direction. We consider each possible value of dip-slip displacement equally likely if it does not exceed 20 cm of reverse slip and 10 m of normal slip: $p(\mathbf{m}) = \mathcal{U}(-0.2\,\mathrm{m}, 10\,\mathrm{m})$. At each cooling step, 300 000 models are explored in parallel by 5000 Markov chains. We do not apply any spatial smoothing regularization with this approach.

4 SLIP MODELS FOR THE AMATRICE EARTHQUAKE

To understand the impact of fault geometry parameters and the influence of epistemic uncertainties on inferred slip models, we first investigate various fault geometries (Section 4.1) and perform synthetic tests (Section 4.2). Then, we solve for slip models of the Amatrice earthquake accounting for uncertainties in the fault geometry (Section 4.3).

The result of our exploration of the model space is a set of 300 000 models describing the posterior likelihood of each dip-slip and strike-slip parameter. This set of samples provides information on the possible parameter values and on their uncertainty. Mean and median models are basic probabilistic values but can give a good overview of the range of most likely solutions. More detailed quantities, such as the marginal posterior distribution of a given parameter or the variability of slip between neighbour subfaults, will inform on the uncertainty and trade-off of the inversion. Yet, the

mere interpretation of average and median samples should be taken with caution: the average model does not reflect the uncertainty of inferred parameters, and it does not reproduce either the interactions between parameters of a same sample.

We choose to present our results in three different ways (e.g. Fig. 2). The first representation is a classic map view of the dip-slip amplitude and rake of the average model (e.g. Figs 2a–b). For the second representation, we divide our 300 000 samples into 25 families of models (more information in Supporting Information Fig. S3). The first family gathers samples with parameters of less than 50 cm offset from the mean model parameters. Other families are built iteratively around a randomly selected model that has not fitted within antecedent families, except for the last family that regroups orphan samples. To have a better understanding of the distribution and interactions between parameters of a particular sample, we then randomly select a sample of each family and illustrate corresponding slip amplitudes (e.g. Figs 2c and d). The last representation (e.g. Fig. 2e) illustrates the posterior marginal PDFs of the dip-slip parameters.

4.1 Influence of fault geometry on inferred slip models

To get a sense of the impact of the fault geometry on inferred models, we compare the results of two inversions made assuming different causative faults, without accounting for uncertainties in the fault geometry. One assumed fault corresponds to our preferred fault geometry, presented in Section 3.2: we will refer to it as fault geometry A. The other fault has the same strike, length and width as our preferred fault geometry but is dipping 5° deeper and is shifted 1.5 km westwards: we will refer to it as fault geometry B. We believe the fault geometry B is almost as realistic as the fault geometry A given the uncertainties on the fault morphology we previously described in Section 2.2.

When assuming fault geometry B, slip is confined in two main slip patches reaching >150 cm of dip-slip amplitude and located between 5 and 10 km depth (Figs 2a and c). The uncertainty on these highest amplitudes can be of more than 50 cm (Fig. 2e and Supporting Information Fig. S4), but the slip patches are well delimited (Fig. 2c). The strike-slip component is limited to ∼5 cm in amplitude in the shallower part of the fault, and is close to zero elsewhere. In contrast, when assuming fault geometry A, while two high-slip patches still stand out, they are smeared out and shifted up-dip (Figs 2b and d). Further, for geometry A, slip amplitudes are generally lower, between 70 and 110 cm (Figs 2b, d and e). The slip tends to be more scattered with larger uncertainties with geometry A (Fig. 2), and the two high-slip patches are thus the only consistent characteristics shared by the two finite-fault slip models. These patches are about 5 km long, and correspond to the large surface displacement patches mapped by InSAR data (Supporting Information Fig. S5). On average, inferred slip amplitudes differ by 75 per cent for slip values >50 cm (Fig. 2e and Supporting Information Fig. S4).

Despite the disparities between the two solutions, both slip models fit the observations almost equally well (Fig. 3 and Supporting Information Figs S5–S8). The largest discrepancies between predictions from the two fault geometries are for data points located between the two assumed fault traces (see RMS values in Supporting Information Table S2). For the ALOS ascending interferogram, residuals between observations and predictions are particularly high when fault geometry B is assumed instead of geometry A (Supporting Information Table S2), consistently with the fact that the choice of geometry A was mainly motivated by the fringe pattern of this interferogram.

In summary, assuming distinct but yet realistic fault geometries results in source models with significant differences but that are almost equally plausible despite very dense near-field observations. Despite the similarities of the two fault geometries, posterior marginal PDFs do not overlap for most of the slip parameters (Fig. 2e). This uncertainty in fault geometry is one of many factors responsible for the non-uniqueness of inferred source models, as illustrated with this example.

4.2 Synthetic tests

We first investigate the relative effect of uncertainties in the fault geometry and crustal properties using synthetic tests. A first target model consists of two 3–4 km large dip-slip patches of 150 cm amplitude, similar to the two main slip patches inferred from our initial models of Amatrice earthquake (Fig. 2). A second target model with inverted slip patches positions (i.e. deep southern slip patch and shallow northern slip patch) is also tested to evaluate the potential influence of the data distribution, which is one major difference with the simplified tests of RSS18 conducted on a semi-infinite fault. Assuming our preferred fault geometry (fault geometry A) and a 1-D layered elastic structure based on the CIA model (Hermann *et al.* 2011), we compute the surface displacement due to our target model (see Fig. 4). This surface displacement is then inverted assuming a dip 10° steeper than the one used to generate the synthetic data and a homogeneous crustal structure. The assumed data covariance $\mathbf{C}_d$ is the same as for the real data set. We perform one inversion with no $\mathbf{C}_p$ (Figs 4c and d), one with $\mathbf{C}_p^{fault}$ (Figs 4e and f) and one with both $\mathbf{C}_p^{fault+earth}$ (Figs 4g and h). The $\mathbf{C}_p^{earth}$ used for the synthetic tests is larger than for the real case because of the large difference between the layered and homogeneous models. We assume a prior standard deviation on fault dip of 5°, of 500 m on the fault position and the prior uncertainty on earth model derives from the observations made in Section 2.2. We choose not to add noise to the observations so that the inversion process is only perturbed by changes in the forward model (fault geometry and earth model) and in the covariance matrix (inclusion of $\mathbf{C}_p$ or not).

The target models and random sampling of possible models are shown in Fig. 4. If $\mathbf{C}_p$ is not accounted for when estimating a slip model mirroring the one of the Amatrice event (Fig. 4c), the slip amplitude in the southern slip patch is either overestimated by 70 cm or underestimated by 50 cm (Fig. 4c). Also, the northern slip patch is shifted upwards with an incorrect estimate of the slip amplitude. When $\mathbf{C}_p^{fault}$ is introduced, the estimation of the target model is slightly improved but is still incorrect (Fig. 4e). These inconsistencies could relate to the assumption of an incorrect earth model, and indeed accounting for $\mathbf{C}_p^{fault+earth}$ allows us to accurately infer the amplitude and location of the target slip model (Fig. 4g). When the target slip model is different (Fig. 4b), again only accounting for $\mathbf{C}_p^{fault+earth}$ allows us to correctly image the slip amplitude and location of the deepest slip patch (Fig. 4h). Quantitatively, the misfit between synthetic observations and predictions follows the same trend as for the Amatrice event: the misfit increases with the introduction of epistemic uncertainties (see Supporting Information Table S2). Finally, we also compare the effect of $\mathbf{C}_p^{fault+earth}$ when the forward model is correct (Fig. 5). In this case, the models inferred accounting or not for epistemic uncertainties are very similar, and the only impact of $\mathbf{C}_p$ is to slightly smooth the slip distribution.

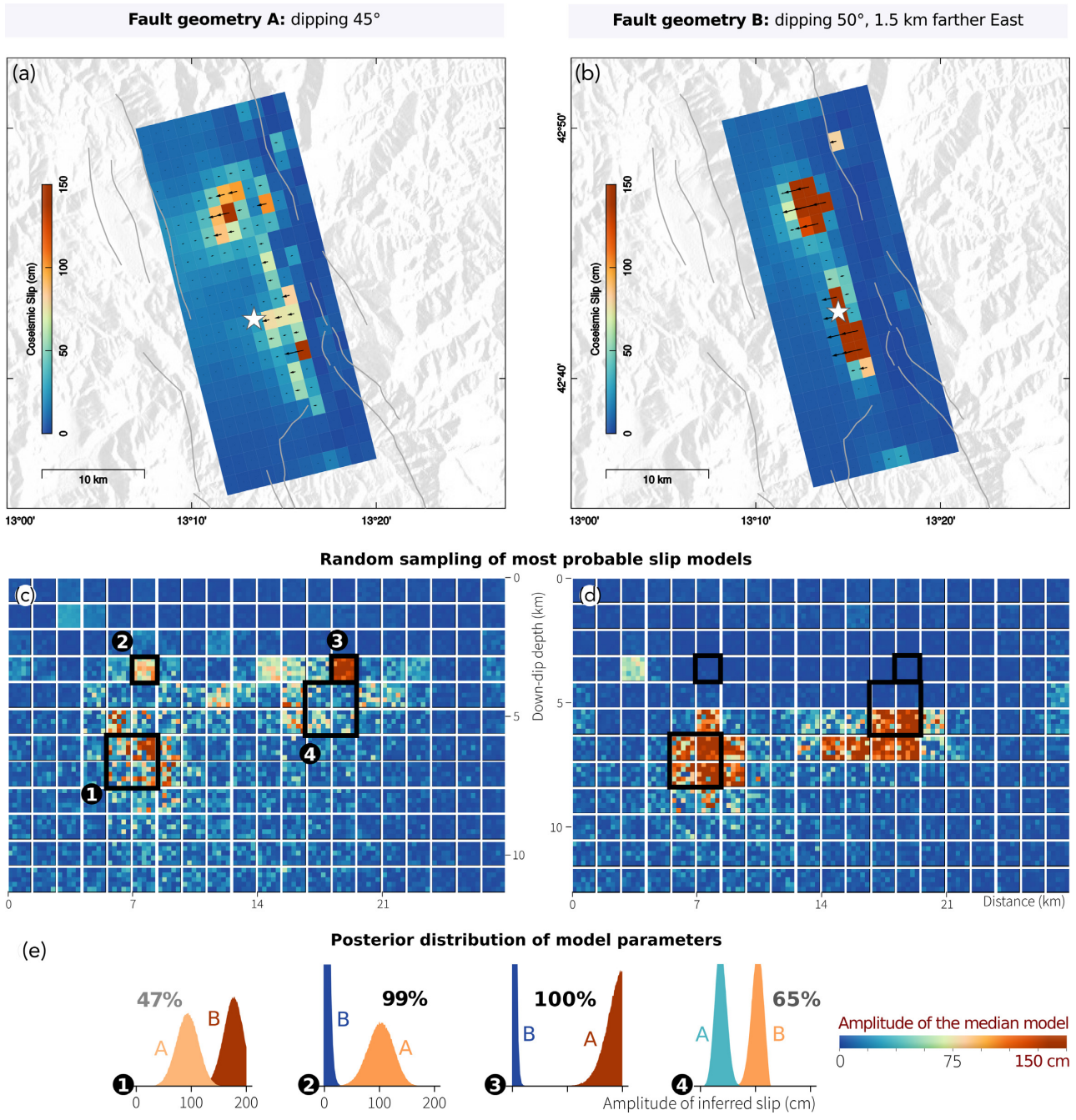

Figure 2. Comparison of two finite-fault slip models inferred assuming different fault geometries and not accounting for prediction uncertainties. Fault geometry A (left) is located 1.5 km west of fault geometry B (right) and is dipping 5° shallower. Panels (a) and (b) show the dip-slip amplitude and rake of the average model, the epicentre being the white star. The colour scale is the same for all the figures. Panels (c) and (d) illustrate the dip-slip amplitude of 25 models chosen randomly among our estimate of possible models. Each subfault (the large square) thus contains 25 pixels with different colours corresponding to the slip amplitude of the random model. (e) Comparison between marginal posterior PDFs of the dip-slip parameters inferred with fault geometry A or B. In (1) and (4), the PDFs show the mean of parameters for patches covering two subfaults along strike and two subfaults along dip—that is, patches two times bigger than in (2) and (3). The offset between mean models is shown as percentage of slip amplitude relatively to the maximum mean slip.

These synthetic tests show that the inclusion of $\mathbf{C}_p$ provides a more reliable estimate of the posterior distribution of source model parameters when the assumed forward model is deficient. The inclusion of $\mathbf{C}_p^{\text{fault+earth}}$ slightly smooths the slip distribution of the deeper patch. The estimates do not perfectly replicate the target model because, even with $\mathbf{C}_p$, the estimated models are still biased to explain the observations despite an incorrect forward model.

4.3 Accounting for uncertainty in fault geometry

We have shown that accounting for uncertainties in the fault geometry allows improving the imagery of the slip distribution, both in the simplified case of an infinitely long fault along strike (RSS18) and in the case of more realistic synthetics tests (see previous Section 4.2). Here, we explore the impact of prediction uncertainty in the estimation for the Amatrice earthquake, by comparing slip

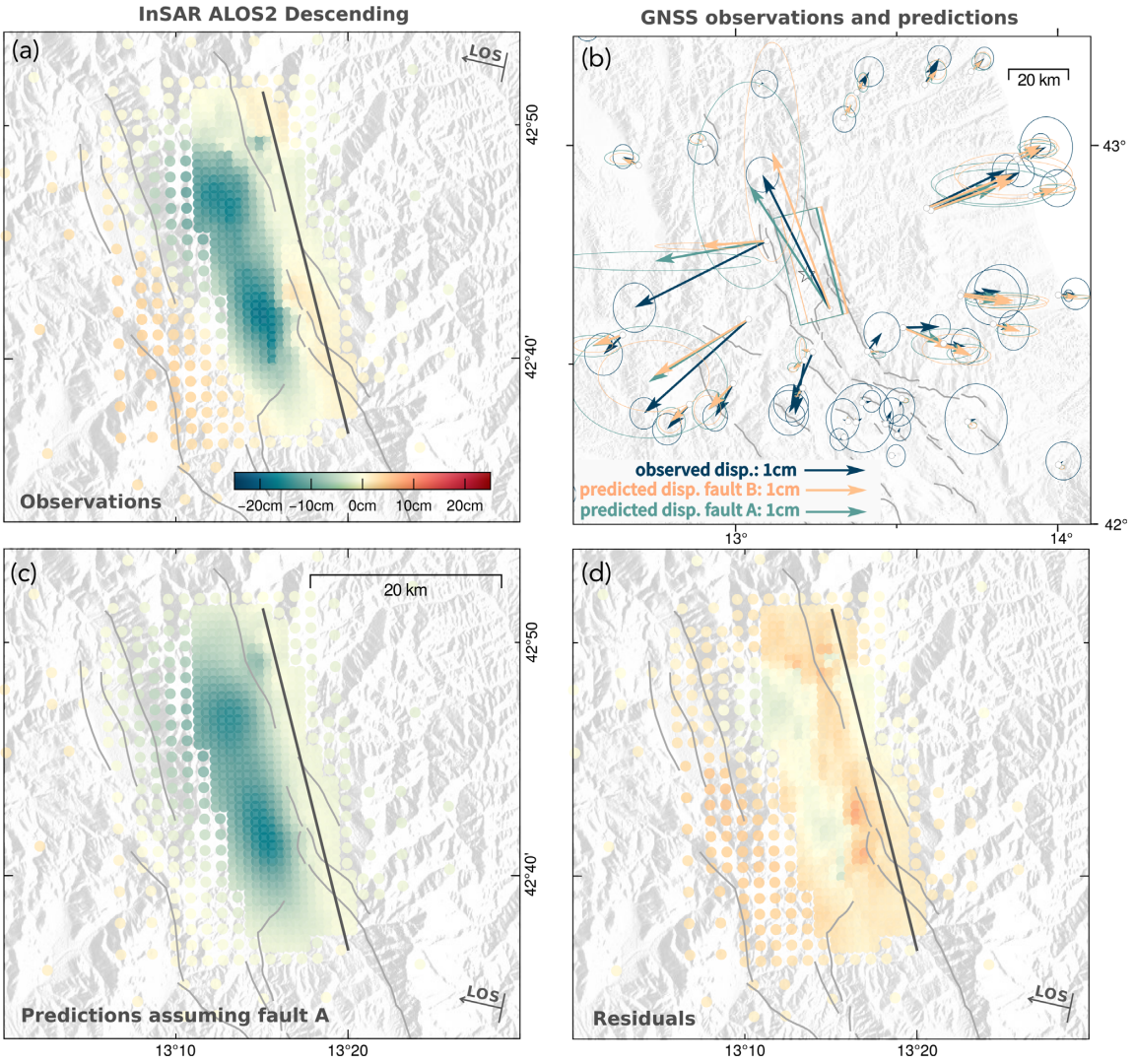

Figure 3. Observations and predictions for our inversion assuming fault geometry A and no epistemic uncertainties. The corresponding slip models are shown in Fig. 2. (a) Surface displacement measured with the ALOS2 interferogram. (b) The surface displacement observed at GNSS stations (top right) is represented by the dark blue arrows with 95 per cent confidence ellipses. The predictions made assuming fault geometry A are in green, and the predictions made assuming fault geometry B are also shown in orange. Surface traces of the fault geometries A and B are, respectively, the green and orange rectangles. (c,d) Predictions and residuals of the ALOS2 interferogram, assuming geometry A, are shown with the same colour scale as in (a). The assumed fault trace (geometry A) is shown with a dark grey line. The predictions for the other three interferograms that have been used in the inversion are shown in Supporting Information Figs S5–S8. In all the figures, major seismogenic faults are shown in the grey solid lines and the epicentre is the white star.

models inferred assuming two different fault geometries (A and B) and accounting for $\mathbf{C}_p^{fault}$.

Fig. 6 shows, for both models, the fault slip is concentrated in two main high-slip patches located between 4 and 9 km depth. The slip direction is pure dip-slip for all subfaults with a significant amount of slip (more than 20 cm). The maximum slip amplitude reaches 150 cm (mean value) for the southern slip patch. Overall, there is little slip on shallow parts of the fault, with less than 40 cm of displacement occurring near the northern tip of the fault, coherently with observed surface ruptures (Fig. 1). Compared to the results inferred without accounting for uncertainties, the slip amplitude of the northern patch is decreased by more than 50 cm or 35 per cent for both fault geometries (Figs 6a and b): this change seems to result from the placement of some of the slip to deeper parts of the fault. Overall, the posterior uncertainty is increased and the posterior standard deviation can be doubled on some subfaults (Figs 6c–e). The variability of possible parameters is better illustrated with an animated slip distribution (see Animated Figs A1 and A2, respectively, without and with $\mathbf{C}_p^{fault}$). When $\mathbf{C}_p^{fault}$ is not accounted for, assuming different fault geometries leads to large variations in inferred slip models with more than 60 per cent offset between average slip amplitudes (Figs 2a and b). In contrast, introducing $\mathbf{C}_p^{fault}$ allows decreasing the offset between the two slip models to less than 40 per cent for most subfaults (Fig. 6e and Supporting Information Fig. S10). Thus, accounting for $\mathbf{C}_p^{fault}$ reduces the discrepancies between models inferred assuming different fault geometries (Figs 6a and b).

Quantitatively, the divergence between two probabilistic distributions can be measured with the Kullback–Leibler divergence criterion. This measure of the divergence also helps characterizing the information gained compared to our initial knowledge of the problem (with no *a priori*, it corresponds to the uniform distribution). If S_i is the posterior distribution of dip-slip for a subfault i, then the

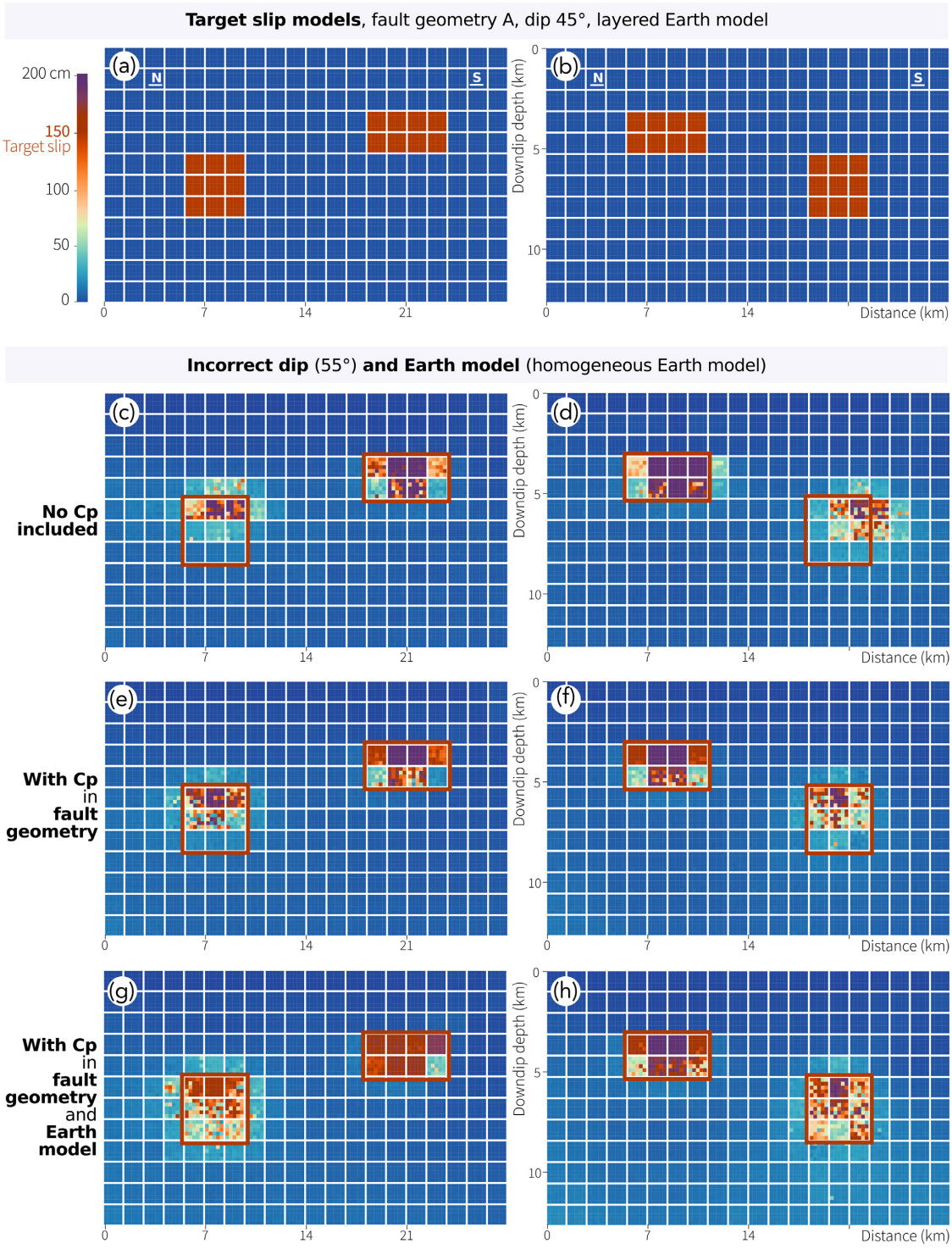

Figure 4. Comparison of finite-fault slip models inferred from two target slip models (a,b) accounting for $\mathbf{C}_p$ in the fault geometry (e,f), in both fault geometry and earth model (g,h), or not (c,d). (a) and (b) show the dip-slip amplitude of the target model used to compute the synthetic observations, assuming fault geometry A and a layered earth model. The colour scale is valid for all the figures. Figures from (c) to (h) illustrate the slip amplitude of the mean models of 25 families of inferred models (more information in Supporting Information Fig. S3). Each subfault (the large square) is divided into 25 pixels coloured from the slip amplitude of the corresponding mean model, inferred assuming an incorrect dip of 10° and homogeneous and elastic earth model. The red rectangles delineate the position of slip patches from target slip models in (a) and (b). The posterior marginal PDFs of models in (c), (e) and (g) are shown in Supporting Information Fig. S9.

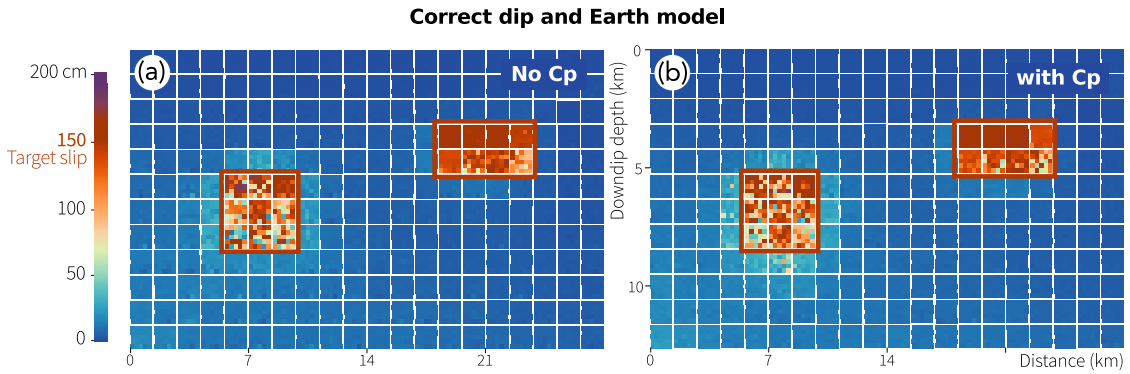

Figure 5. Comparison of finite-fault slip models inferred from the target slip model illustrated in Fig. 4(a), assuming the correct forward model (i.e. the same forward model used to calculate the synthetic data). Panel (a) shows the model inferred without accounting for uncertainties, but the model in (b) has been inferred with $\mathbf{C}_p^{\text{fault+earth}}$. The red rectangles delineate the position of slip patches from target slip models in Figs 4(a) and (b).

entropy of S_i relative to the uniform distribution $\mathcal{U}$ is

$$E(S_i||\mathcal{U}) = \sum_j S_i(j) \log \frac{S_i(j)}{\mathcal{U}(j)}, \tag{7}$$

with j describing the number of possible values of the distribution (or the bins of the histogram). We normalize the relative entropy by its largest value. When the normalized relative entropy is close to 1, the distributions are divergent and the information gained relative to the prior distribution is large. If the entropy is close to 0, then the posterior and prior distributions are similar and the information gain is small or null. The distributions of parameters inferred assuming fault geometry B diverge largely from the distributions inferred with fault A when $\mathbf{C}_p^{\text{fault}}$ is not accounted for (Fig. 7a). In contrast, the relative entropies between parameters of models inferred assuming different fault geometries is decreased by a factor of 2 if $\mathbf{C}_p^{\text{fault}}$ is introduced (Fig. 7b). Interestingly, Figs 7(c) and (d) show that the information gain is larger in area where little slip is inferred, than inside the high-slip areas. Thus, the observations constrain well the areas with no slip, but are not sufficient to infer the amplitude of slip where it is the largest. Around the potential deep slip patch, the introduction of uncertainties makes the information gain to decrease to very small values. In other words, regarding the possible inaccuracies of our assumed forward model, we cannot evaluate if this deep patch slipped largely, moderately or not at all. Overall, when accounting for uncertainties in the fault geometry, the information gained from our initial knowledge is slightly reduced because the posterior uncertainty is increased—and posterior distributions are closer to the uniform distribution (Figs 7c and d). Yet, the residuals between dip-slip amplitudes of the average models show that all subfaults are impacted by the inclusion of $\mathbf{C}_p^{\text{fault}}$, regardless of their slip amplitude (Supporting Information Fig. S11). On average, accounting for $\mathbf{C}_p^{\text{fault}}$ modifies by 40 per cent the slip amplitude of area characterized by large slip (>50 cm; Supporting Information Fig. S11).

As expected, predictions of the average model inferred with $\mathbf{C}_p^{\text{fault}}$ have a larger misfit with observations than if $\mathbf{C}_p^{\text{fault}}$ is neglected (see Fig. 8 and Figs S7, S8, S12, S13 and Supporting Information Table S3). But again, the better fit to the data with no $\mathbf{C}_p$ is simply the consequence of assuming perfect knowledge of the fault geometry. For the GPS data, the ability to predict the observations depends on the location of the stations, with a better prediction when $\mathbf{C}_p^{\text{fault}}$ is accounted for (Fig. 8).

In summary, accounting for $\mathbf{C}_p^{\text{fault}}$ reduces the sensitivity of inferred models to different assumptions in the fault geometry. Additionally, the introduction of uncertainties in the fault geometry does not influence the general slip pattern consisting of two main slip patches, but significantly increases the probability that some slip occurred on the deepest subfaults and also increases the posterior uncertainty at depth. The synthetic tests we perform in Section 4.2 show that the inclusion of $\mathbf{C}_p^{\text{fault}}$ is not responsible for the inference of slip at depth for the Amatrice earthquake. We thus interpret the inferred deep slip of the Amatrice event as realistic albeit at low spatial resolution, given our imperfect knowledge of the fault geometry.

4.4 Accounting for uncertainties in both fault geometry and earth model

Fault geometry parameters are not the only parameters that are held fixed in source estimation problems. Earth structure is often chosen *a priori* despite being an important source of epistemic uncertainty (e.g. Beresnev 2003; Duputel *et al.* 2014). And just as with fault geometry, Earth structure is almost never known perfectly. We thus investigate the impact of accounting for uncertainties in both fault geometry and Earth structure and evaluate if one appears more critical than the other. Our results show that the inferred models are very similar whether $\mathbf{C}_p^{\text{earth}}$ is included or not when assuming fault geometry A (Supporting Information Fig. S14). We only note that the additional introduction of $\mathbf{C}_p^{\text{earth}}$ appears to better isolate the two main slip patches, while slightly decreasing the slip amplitude inferred at deeper parts of the fault (Supporting Information Fig. S14). Previous synthetic tests (Section 4.2, RSS18) have shown that when both assumed fault geometry and earth model are incorrect, only the inclusion of the two types of uncertainties allows to approach the target model. Yet, for the Amatrice earthquake, the inclusion of $\mathbf{C}_p^{\text{fault+earth}}$ has a limited impact on the results compared to the inclusion of $\mathbf{C}_p^{\text{fault}}$ only.

5 DISCUSSION

5.1 Influence of uncertainties in the fault geometry

Our synthetic tests show that if uncertainties in the fault geometry are not accounted for, assuming an incorrect fault dip leads to spurious effects on the inferred model. In contrast, accounting for $\mathbf{C}_p^{\text{fault}}$ improves the estimation of the target model even if the assumed

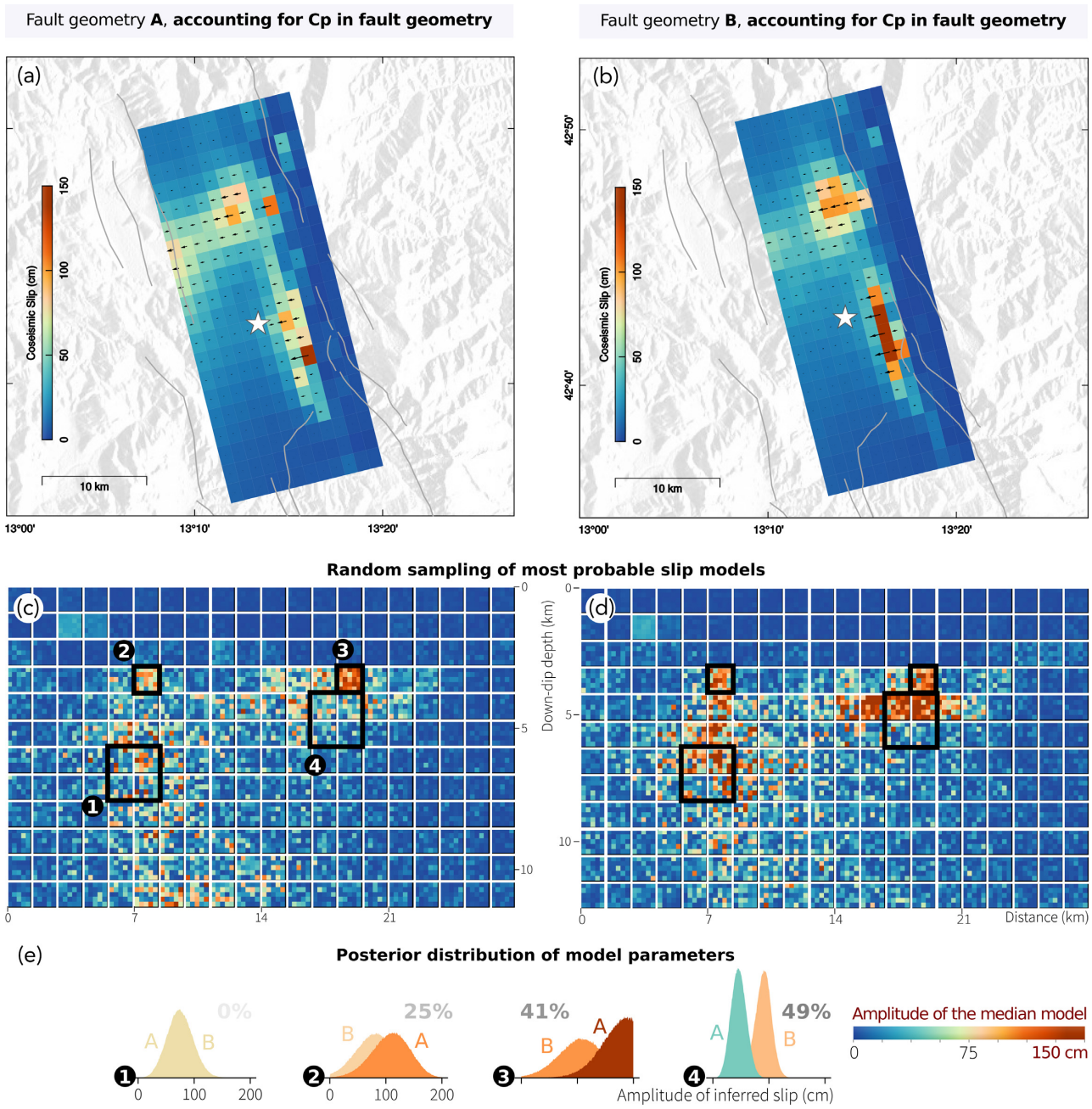

Figure 6. Comparison of two finite-fault slip models inferred accounting for uncertainties in fault geometry, for fault geometry A (left) and B (right). Panels (a) and (b) show the dip-slip amplitude and rake of the average model, the epicentre being the white star. The colour scale is valid for all the figures. Panels (c) and (d) illustrate the slip amplitude of 25 samples chosen randomly among the possible models. Each subfault (the large square) thus contains 25 pixels with different colours corresponding to the slip amplitude of the random model. (e) Comparison between posterior marginal PDFs of the dip-slip parameters inferred with fault geometry A or B. In (1) and (4), the PDFs show the mean of parameters for patches covering two subfaults along strike and two subfaults along dip—that is, patches two times bigger than (2) and (3). The offset between mean models is shown as percentage of slip amplitude relatively to the larger mean slip.

fault dip and earth model are incorrect. When accounting for the uncertainties in fault geometry, inferred models thus reflect what we can reliably infer given our imperfect knowledge of the forward model (assuming the rest of the forward model is correct).

More importantly, we show with the Amatrice earthquake that accounting for uncertainties in the fault geometry makes inferred models less sensitive to a variation in assumed fault geometry. If $\mathbf{C}_p^{\text{fault}}$ is introduced in the inversion process, our assumption of the forward model has less impact on finite-fault source models. Yet, our approach has its limits (in particular the linearization to derive $\mathbf{C}_p$), and the choice of a realistic fault geometry is still critical to infer a realistic model. In summary, when there is ambiguity about the fault geometry, which will always be the case to some extent, we show that the inclusion of $\mathbf{C}_p^{\text{fault}}$ improves the robustness of the solution.

$\mathbf{C}_p$ encapsulates the uncertainty related to the deficiencies of our assumed forward model. For most earthquakes, the impact of $\mathbf{C}_p$

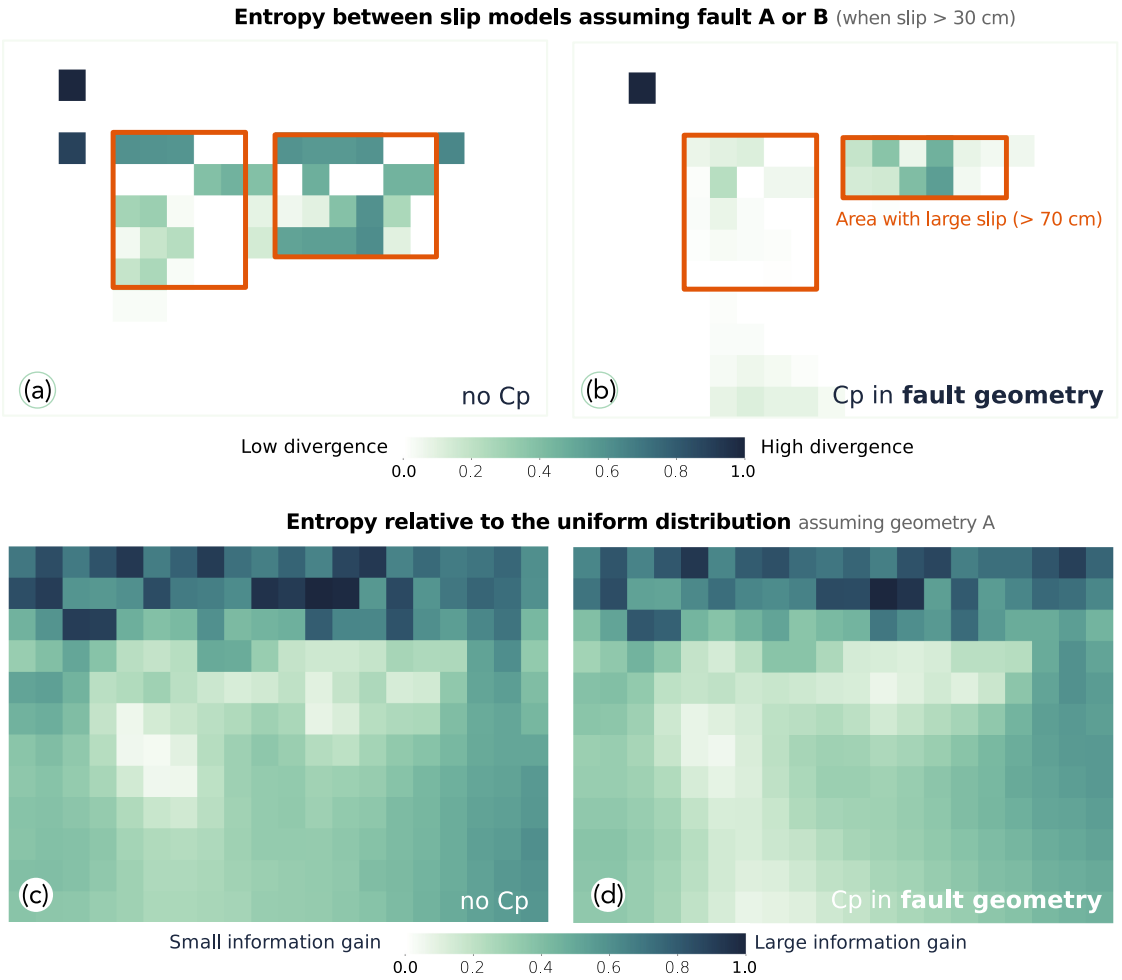

Figure 7. (a,b) Relative entropies between dip-slip distributions of models inferred assuming fault geometry A and fault geometry B, without $\mathbf{C}_p$ (a) or with $\mathbf{C}_p$ (b). In (a), compared models are illustrated in Fig. 2, while the models in (b) are represented in Fig. 6. The entropy reflects the divergence between the distributions of parameters of two models. If S_i is the dip-slip posterior distribution for a subfault i, then the relative entropy between the posterior distributions inferred accounting or not for $\mathbf{C}_p$ is $E(S_i^{C_p}||S_i) = \sum_j S_i^{C_p}(j) \log S_i^{C_p}(j)/S_i(j)$. (c,d) Entropy relative to the uniform distribution for an inversion assuming fault geometry A, without $\mathbf{C}_p$ (c) or with $\mathbf{C}_p$ (d).The relative entropies in (a), (b), (c) and (d) are normalized by their largest value.

will vary with the sensitivity of the model parameters to the assumed forward physics. But this sensitivity will also depend on other assumed characteristics of the forward problem, such as data distribution or assumed fault resolution, as we show with our synthetic tests. The influence of $\mathbf{C}_p$ will thus be difficult to anticipate. Additionally, a trade-off may exist between different assumptions of the forward model. For instance, the model parameters may be less sensitive to a variation in the fault geometry if both fault dip and position vary so that the peak slip location remains unchanged. Similarly, a change in both fault dip and position may induce variations in the surface predictions larger than if only one parameter is changed. In our study, we considered independent variations of fault geometry parameters to estimate the uncertainties in the predictions, in order to separate the relative effect of parameters of the forward model. Yet, we could also investigate more complex changes in fault geometry to limit the trade-off between estimated uncertainties: variations of both fault dip and position, both fault strike and position or also fault dip and Earth elastic properties.

Our study shows that assuming different fault geometries allows to solve the inverse problem with a similar fit to the observations. This result is consistent with the variability of proposed fault geometries in published slip models of the Amatrice earthquake (references therein). Most of these geometries have been inverted (Bonini *et al.* 2016; Cheloni *et al.* 2016; Lavecchia *et al.* 2016; Tinti *et al.* 2016; Huang *et al.* 2017b; Liu *et al.* 2017; Tung & Masterlark 2018). The variability of inferred fault geometries can result from the type of inverted observations, the chosen parametrization of the forward model or simply because of the non-uniqueness of this inverse problem. But such variability can also be related to the uncertainties of non-inverted parameters of the forward model, if related uncertainties are not accounted for (RSS18). For instance, Tung & Masterlark (2018) solve for all the parameters describing the fault geometry, but also show these parameters trade-off with the assumed earth model. While many studies solve for the fault geometry only (e.g. Fukahata & Wright 2008; Fukuda & Johnson 2010; Sun *et al.* 2011; Huang *et al.* 2017a; Marchandon *et al.* 2018), they do not account for any trade-off or for the uncertainty of parameters that are not inverted for, such as the fault position or earth model. Yet, to infer a robust solution the uncertainty of all parameters describing the forward model, and which are not inverted for, should probably be estimated.

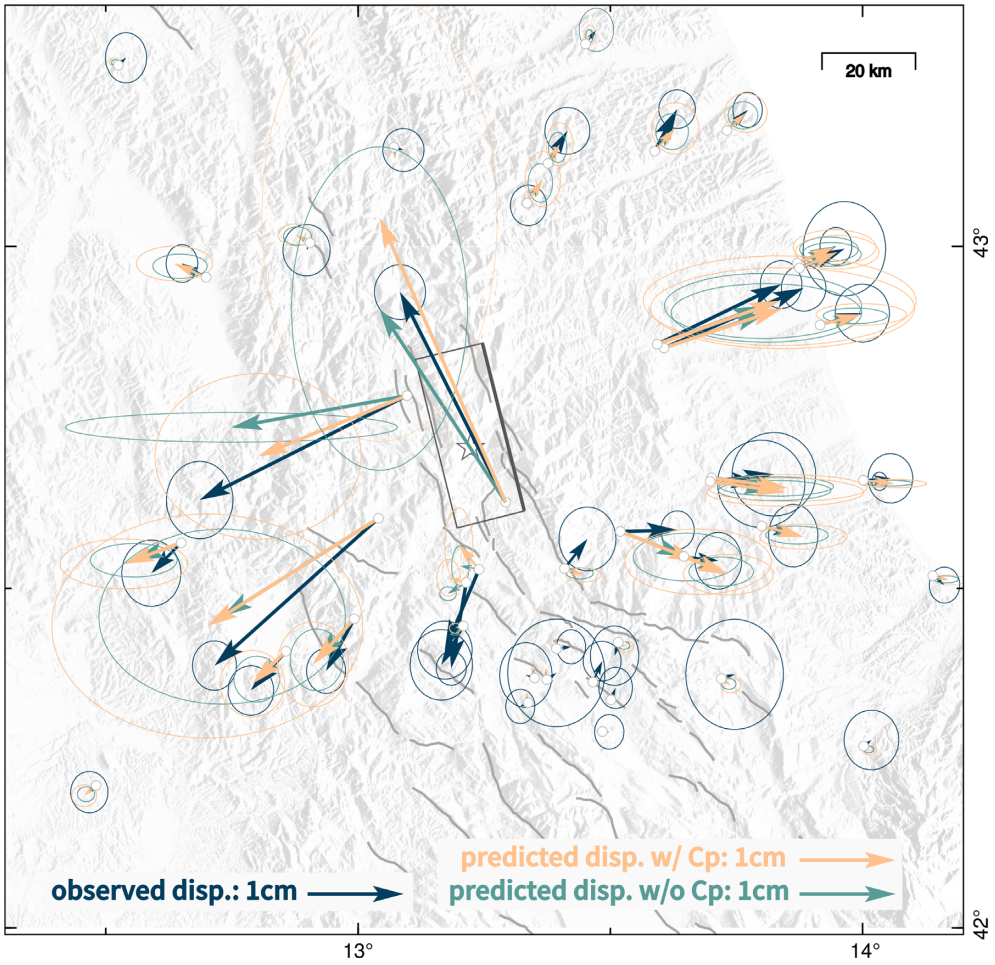

Figure 8. Surface displacement at GPS stations, for slip models accounting (orange) or not (green) for uncertainties in fault geometry (slip models are presented in Fig. 6). Observed surface displacement is in dark blue with 95 per cent confidence ellipses. Major seismogenic faults are shown in the grey solid lines and the epicentre is the white star. The black rectangle is the location of our fault plane (geometry B).

5.2 Discussion of the co-seismic models of the Amatrice earthquake

Our preferred slip model of the Amatrice earthquake, inferred accounting for epistemic uncertainties, shows large dip-slip amplitudes restricted to a narrow band located between 3 and 7 km depth (below sea level; Fig. 9). There is almost no slip imaged in the along-strike direction. The co-seismic slip is distributed in two main slip patches, with maximum amplitudes of 150 cm being reached in the southern part of the fault. These main characteristics are shared by most of published source models (e.g. Tinti *et al.* 2016; Cheloni *et al.* 2017; and references therein). Additionally, our probabilistic approach, along with a detailed evaluation of uncertainties, allows us to enhance our image of the co-seismic slip, and obtain a broader picture of possible source models. Two main distinct slip asperities ruptured co-seismically, with almost no slip inferred in between (as imaged by Tinti *et al.* 2016; Lavecchia *et al.* 2016; Chiarabba *et al.* 2018). While the southern part of the fault has been ruptured by high-slip amplitudes confined to a narrow zone, the slip is more distributed towards the north and shallow slip (1–2 km depth) is imaged below the surface rupture observed along the Mt Vettore (reaching 20 cm offset, Fig. 1). Additionally, in the northern part of the fault, slip may have occurred around 8–9 km depth, reaching up to 1 m of amplitude. We also confirm that the co-seismic slip have

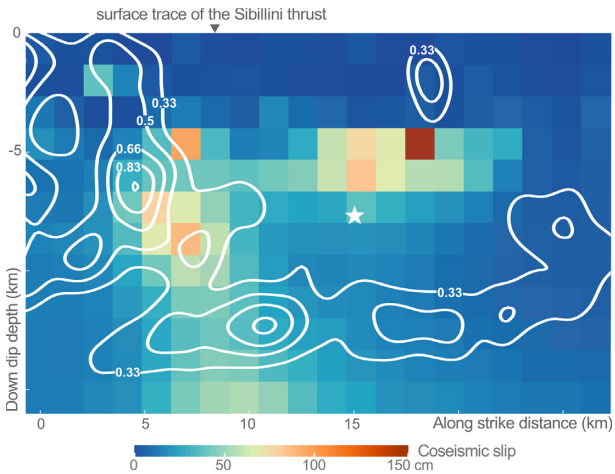

Figure 9. Our preferred model of dip-slip amplitude (mean model of an approach assuming fault geometry A and $\mathbf{C}_p^{\text{fault+earth}}$) on which is superimposed the normalized density of aftershocks that occurred until October 2016 (catalogue of Chiarabba *et al.* 2018). The density of aftershocks located within 3 km of the fault (to account for potential uncertainty of the fault geometry) is calculated with a kernel density estimation method (Parzen 1962) with a smoothing factor of 0.6. The mainshock is the white star.

not propagated above 3 km depth, at the exception of the neighbourhood of the Mt Vettore. This deficit of slip in shallow parts of the fault has also been modelled by several authors (e.g. Lavecchia *et al.* 2016; Chiaraluce *et al.* 2017; Huang *et al.* 2017b; Liu *et al.* 2017; Pizzi *et al.* 2017), although not as clearly as in our slip model.

Most of the characteristics of the co-seismic rupture of the Amatrice event could be related to the impact of inherited structures. The structural framework of central Italy is impacted by the interactions between inherited thrust faults and extensional faults (e.g. Chiaraluce *et al.* 2005; Pizzi & Galadini 2009). In particular, the inherited Sibillini thrust may separate the northern and southern parts of the causative fault of the Amatrice event (Figs 1 and 9), or may delimit the causative fault in its northern part (Chiarabba *et al.* 2018), and have already been invoked to act as a structural barrier for the 2016 seismic sequence (e.g. Bonini *et al.* 2016; Pizzi *et al.* 2017). South of the Sibillini thrust, most of the slip is located deeper than 3 km, a depth corresponding to the thickness of the sediment pile (deposited from Jurassic to Messinian times; e.g. Bonini *et al.* 2016; Pizzi *et al.* 2017). The sediment pile may have prevented the co-seismic rupture to reach shallower depths. The causative fault thus probably stops at 2–3 km below the sea level (Fig. 1). This hypothesis is supported by the fact that very few observations of surface rupture have been made in this area (Pucci *et al.* 2017). Additionally, very few aftershocks are located shallower than 3–4 km depth in the southern part of the fault (Fig. 9). In contrast, in the northern part of the causative fault, both co-seismic rupture and aftershocks reach the surface (Fig. 9). The northern part of the fault may be located north of the Sibillini thrust, where most of the sediment pile have been eroded, allowing for shallow rupture.

Still in the northern part of the fault, the potential slip at depth may have been favoured by the Sibillini thrust, and/or may also be the result of afterslip. Indeed, the InSAR data that have been used to image the co-seismic rupture are contaminated by a few days of post-seismic deformation. Many aftershocks including an M_w 5.4 event occurred in this area (Figs 1 and 9), and the locations of aftershocks and afterslip may correlate, as modelled for the 2009 L'Aquila earthquake (e.g. D'Agostino *et al.* 2012; Cheloni *et al.* 2014). Supporting Information Fig. S15 advocates that the data, and particularly the descending interferograms, may require this deep slip to explain a low-signal deformation occurring just around the location of the M_w 5.4 aftershock. The potential deep slip may thus correspond to the co-seismic slip of the M_w 5.4 aftershock. The moment magnitude of a fault area slipping of 75 cm at depth (Model 2 in Supporting Information Fig. S15) corresponds to an M_w 5.75. When considering uncertainties on the elastic modulus (μ could vary between 2.5 and 4.5 GPa), the slip amplitude (varying between 40 and 90 cm) and the surface that slipped, the moment magnitude of the potential slip may vary between 5.35 and 5.95. On the other hand, the loss of information gain when introducing $\mathbf{C}_p$ (Figs 7 c and d) suggests the data are not sufficient to constrain this potential slip at depth, and that the fault geometry may not be realistic in this part of the fault. The lineament defined by the aftershocks at 8–10 km depth (Fig. 9) has been interpreted by several authors to be a low-angle fault (e.g. Chiaraluce *et al.* 2017; Lavecchia *et al.* 2017), on which the active normal faults take root. Thus, the slip imaged at ∼10 km depth may also be located on this low-angle fault, which may have hosted creep deformation (as also suggested by Chiaraluce *et al.* 2017). In summary, we cannot specifically conclude if the potential slip at depth results from the co-seismic rupture of the M_w 5.4 aftershock, from a creep episode on the low-angle fault, or from both.

5.3 Is $\mathbf{C}_p^{fault}$ always critical in finite-fault slip inversions?

As shown in Section 4.4 and Supporting Information Fig. S14, the additional inclusion of $\mathbf{C}_p^{earth}$ has a limited impact on the inferred models compared to the introduction of $\mathbf{C}_p^{fault}$ only. This lack of influence could result from two effects: either our calculated uncertainty in crustal structure is of limited amplitude or once a particular epistemic uncertainty threshold has been reached, adding more uncertainties is of little effect. To test these two hypotheses, we conduct additional inversions modulating the contribution of the $\mathbf{C}_p$ terms: $\mathbf{C}_p^{fault}$ only, $\mathbf{C}_p^{earth}$ only, $\mathbf{C}_p^{dip}$ only, $\mathbf{C}_p^{fault+earth}$ and a doubled $\mathbf{C}_p^{fault+earth}$ (Fig. 10 and Supporting Information Fig. S16). The comparison of these different tests indicates that the introduction of any amount of epistemic uncertainty only impacts the two main slip patches, increasing the posterior uncertainty and smoothing the slip distribution over surrounding subfaults (Fig. 10 and Supporting Information Fig. S16). The increase of posterior uncertainty is particularly evident for subfaults found to experience the largest slip (Supporting Information Fig. S16). Models inferred with $\mathbf{C}_p^{fault}$ only or $\mathbf{C}_p^{earth}$ are very similar (Figs 10c and d), as are models inferred accounting for large uncertainties: $\mathbf{C}_p^{fault+earth}$ or a $\mathbf{C}_p^{fault+earth}$ matrix with twice the amplitude (Figs 10e and f). If we account for a small amount of uncertainty (Fig. 10b), inferred model mirrors the one imaged with $\mathbf{C}_p^{fault}$ except that no slip is imaged at depth. The impact of $\mathbf{C}_p^{fault}$ or $\mathbf{C}_p^{earth}$ is thus different but of similar amplitude. Yet, when both epistemic uncertainties are included in the inversion process, or when the amplitude of the $\mathbf{C}_p$ matrix is doubled, we do not observe as much change in slip models. For the Amatrice earthquake, going beyond a certain amount of epistemic uncertainties has little influence on the imaged slip. This amount appears to be reached when uncertainties in fault dip, position and earth model are introduced.

This result implies that the introduction of additional or more sophisticated uncertainties in fault geometry, such as uncertainties related to complex structures (such as fault bends and multiple segments), is probably not particularly justifiable. For most earthquakes, accounting for complex parameters might only become critical if basic parameters (such as fault dip, strike and position) are well constrained, and if there is evidence of specific features (e.g. listric fault, multiple branching) that could strongly affect the Green's functions. Similarly, accounting for additional uncertainties related to the data distribution or assumed fault resolution is likely dispensable for most studies.

Additionally, as discussed in RSS18, the impact of uncertainty in fault geometry, and of $\mathbf{C}_p$ in general, depends on the data distribution. Near-fault observations will be particularly impacted by a change in fault morphology, while far-field data are less sensitive to a deficiency of the assumed fault geometry. The inclusion of $\mathbf{C}_p$ will thus be particularly efficient for the imagery of continental earthquakes, for which data can be acquired very close to the fault. For subduction earthquakes, for which observations tend to be located relatively far from the rupture (e.g. more than 100 km), the impact of $\mathbf{C}_p$ may be limited. Yet, for subduction earthquakes for which some data are distributed close to the trench, such as the M_w 9.1 2004 Sumatra–Andaman earthquake or the M_w7.8 2016 Pedernales earthquake, which occurred mainly along coastlines or islands, the influence of $\mathbf{C}_p$ may help infer more robust models.

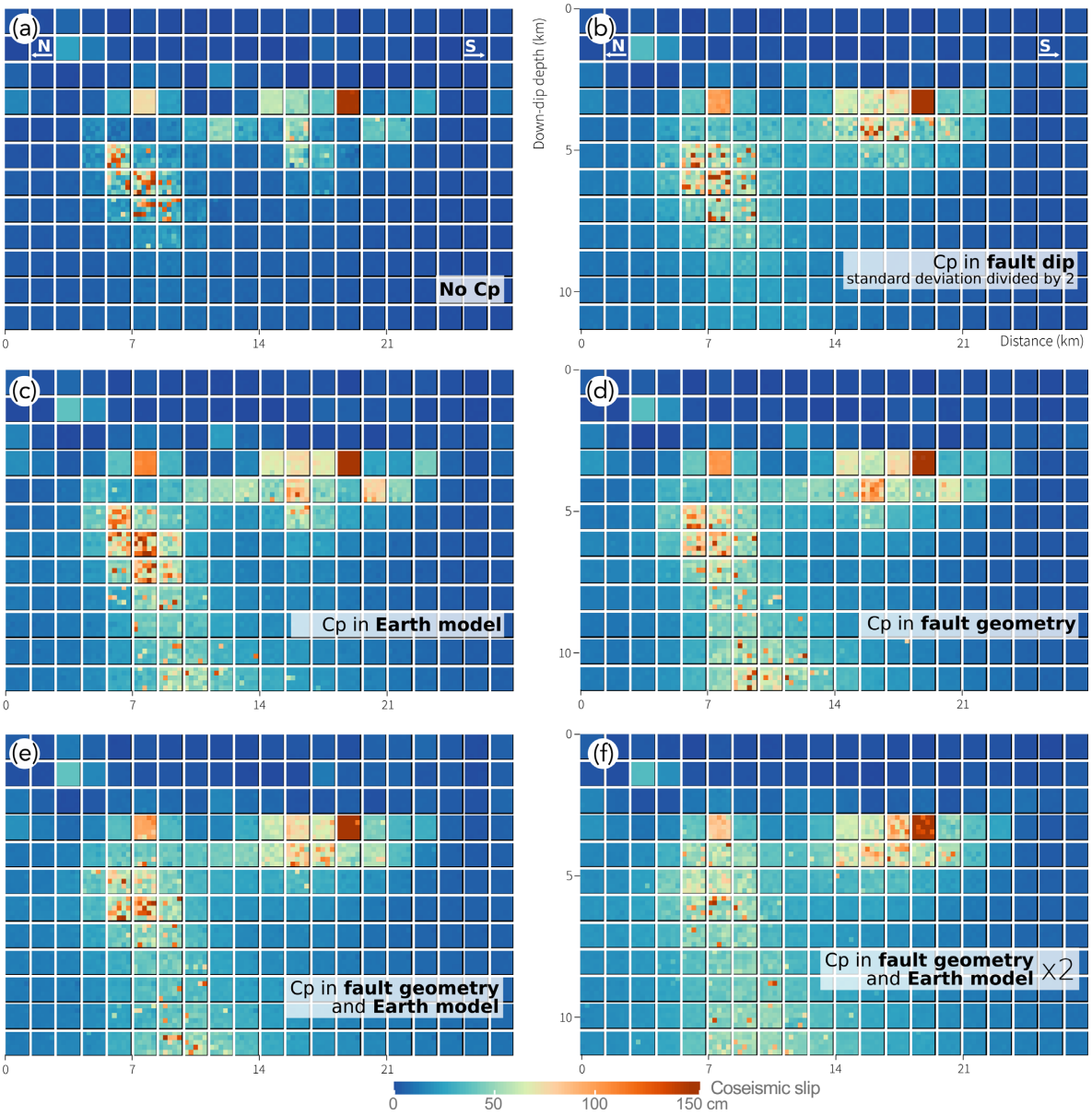

Figure 10. Comparison of finite-fault slip models inferred accounting for different $\mathbf{C}_p$ matrices (b–f) or not (a). Figures illustrate the average dip-slip amplitude of 25 families of models, inferred assuming fault geometry A and a layered earth model. (a) No $\mathbf{C}_p$ is accounted for (same model as in Fig. 2a). (b) Only $\mathbf{C}_p^{dip}$ is included, and the matrix has been computed with a prior standard deviation of 2.5°. (c) Only $\mathbf{C}_p^{earth}$ is introduced. (d) Only $\mathbf{C}_p^{fault}$ is accounted for (same model as in Fig. 6a). (e) Both $\mathbf{C}_p^{fault}$ and $\mathbf{C}_p^{earth}$ are accounted for (same model as in Supporting Information Fig. S14). (f) Both $\mathbf{C}_p^{fault}$ and $\mathbf{C}_p^{earth}$ are accounted for such that $\mathbf{C}_p = 2 \times (\mathbf{C}_p^{fault} + \mathbf{C}_p^{earth})$.

6 CONCLUSIONS

Although observational errors are usually accounted for in static source inversions, the uncertainties associated with potential deficiencies of the forward model are generally ignored. Yet, uncertainties of the forward model, derived from our assumed crustal properties, topography or fault morphology, can be 10^3 to 10^6 times larger than observational errors for well recorded great earthquakes ($M_w > 8$; Ragon *et al.* 2018).

In this study, we investigated the impact of uncertainties in fault geometry for a real event. We first have ensured our proposed formalism works for the very simple case of a semi-infinite fault, to put aside any effect due to 3-D complexity (Ragon *et al.* 2018). Here, we test and apply our approach to the M_w 6.2 Amatrice earthquake, Italy, a well-observed event characterized by a relatively simple fault morphology that allows to focus on first-order fault geometry parameters, such as fault dip and position. We draw the following conclusions from synthetic tests and from a comparison of several slip models, inferred with distinct fault geometries and accounting or not for related uncertainties. We demonstrate that the introduction of uncertainty in fault geometry reduces the sensitivity of inferred models to a variation in fault geometry. Thus, accounting for $\mathbf{C}_p$ helps infer more robust source models, even for this earthquake whose moderate size will not exacerbate the role of epistemic uncertainties (as the amplitude of epistemic uncertainties scales with slip). In essence, accounting for epistemic uncertainties

is like rescaling the fit to the observations such that more weight is put on observations that the forward problem can predict more robustly. That way, when uncertainties are included, we ensure that inferred models reflect what we can realistically infer given our knowledge of the Earth's interior.

While it is necessary to include uncertainties in both fault geometry and crustal structure to infer reliable models, we also show that accounting for multiple uncertainties is only critical up to a certain point. For most continental earthquakes, the estimation of first-order epistemic uncertainties (e.g. layered earth model and fault dip, position or strike) will be sufficient to ensure that the inferred static models are realistic enough. It may also be necessary to explore the uncertainties of 3-D Earth structure for some earthquakes, for instance, in subduction zones. Accounting for more complex uncertainties, such as deriving from fault segmentation, bend or roughness, will only become critical if a particular complex parameter has a substantial influence. Indeed, the Amatrice earthquake is well instrumented and the elementary epistemic uncertainties are rather small, and yet the introduction of basic uncertainties causes significant changes in the inferred models. The inclusion of $\mathbf{C}_p$ in the inversion process will be particularly significant for earthquakes with near-fault observations, such as continental events.

Finally, $\mathbf{C}_p$ is not limited to static problems. In this study (and in Ragon *et al.* 2018), we focused on the inversion of geodetic data. $\mathbf{C}_p^{\text{fault}}$ derives from the sensitivity of the Green's functions to the fault geometry. Because of the relative simplicity of the static Green's functions, we determine their sensitivity from a linear regression. For a waveform inversion, the Green's functions become also function of time. Yet, a similar approach can be applied: the sensitivity of the time-dependent Green's functions to the fault geometry can be derived from the direct comparison of the functions. For instance, to investigate the influence of a specific fault geometry parameter, one can use the *p*-norm of the difference between two Green's functions computed for two values of this parameter. Although this approach is more computationally demanding than for the static case, to account for uncertainties in fault geometry in waveform inversion procedures can have a significant impact on inferred models. One could also follow an approach similar to the one used by Jiang & Simons (2016) to account for the uncertainties in tsunami propagation associated with wave dispersion characteristics. Some methodologies have already been proposed for waveform finite-fault inversions: to account for uncertainty of Green's functions (Yagi & Fukahata 2011), which can be derived from the residuals between predictions and observations (Dettmer *et al.* 2014, 2016), uncertainty in source time functions and Earth structure (Razafindrakoto & Mai 2014), to estimate uncertainty related to Earth structure (Hallo & Gallovic 2016) or centroid location (Duputel *et al.* 2012). Duputel *et al.* (2015) accounted for uncertainties in the elastic structure of the Earth for both geodetic and seismic data. Yet, none of these methodologies allow to include uncertainties in fault geometry for inversion of both static and kinematic observations.

ACKNOWLEDGEMENTS

We thank Q. Bletery, B. Gombert and Z. Duputel for helpful discussions. We thank C. Liang, M.H. Huang and E. Fielding for providing us their processed ALOS-2 interferograms, original ALOS-2 data being copyright by Japan Aerospace Exploration Agency (JAXA) and provided under JAXA ALOS RA-4 projects (S.H. Yun) and P1372 (E. Fielding). The Sentinel-1 original images contain modified Copernicus data, and have been processed within the ARIA project, NASA/JPL-Caltech. We thank Claudio Chiarraba and Pasquale De Gori for provinding their catalogue of aftershocks (Chiarabba *et al.* 2018). The Bayesian simulations were performed on the HPC-Regional Center ROMEO (https://romeo.univ-reims.fr) of the University of Reims Champagne-Ardenne (France). The Classic Slip Inversion Python library created by Romain Jolivet (Jolivet *et al.* 2015) was used to build inputs for the Bayesian algorithm and to perform the optimization of the inverse problem. Figures were generated with the Matplotlib and Seaborn Python libraries. This study was partly supported by the French National Research Agency (ANR) EPOST project ANR-14-CE03-0002. TR is supported by a fellowship from the French Ministry of Research and Higher Education. MS was supported by U.S. National Science Foundation grant 1447107.

A simple version of the code used to calculate the uncertainties in assumed fault dip, strike and position can be freely downloaded at `github.com/thearagon/epistemic_uncertainties`.

REFERENCES

Ameri, G., Gallovič, F. & Pacor, F., 2012. Complexity of the M_w 6.3 2009 L'Aquila (central Italy) earthquake: 2. Broadband strong motion modelling, *J. geophys. Res.,* **117**(B4), B04308, doi:10.1029/2011JB008709.

Bagh, S., Chiaraluce, L., De Gori, P., Moretti, M., Govoni, A., Chiarabba, C., Di Bartolomeo, P. & Romanelli, M., 2007. Background seismicity in the central Apennines of Italy: the Abruzzo region case study, *Tectonophysics,* **444**(14), 80–92.

Beresnev, I.A., 2003. Uncertainties in finite-fault slip inversions: to what extent to believe? (a critical review), *Bull. seism. Soc. Am.,* **93**(6), 2445–2458.

Bianchi, I., Chiarabba, C. & Piana Agostinetti, N., 2010. Control of the 2009 L'Aquila earthquake, central Italy, by a high-velocity structure: a receiver function study, *J. geophys. Res.,* **115**(B12), B12326, doi:10.1029/2009JB007087.

Boncio, P., Lavecchia, G., Milana, G. & Rozzi, B., 2004a. Seismogenesis in central Apennines, Italy: an integrated analysis of minor earthquake sequences and structural data in the Amatrice-Campotosto area, *Ann. Geophys.,* **47**(6), 1723–1742.

Boncio, P., Lavecchia, G. & Pace, B., 2004b. Defining a model of 3D seismogenic sources for Seismic Hazard Assessment applications: the case of central Apennines (Italy), *J. Seismol.,* **8**(3), 407–425.

Bonini, L. *et al.*, 2016. Imaging the tectonic framework of the 24 August 2016, Amatrice (central Italy) earthquake sequence: new roles for old players? *Ann. Geophys.,* **59,** doi:10.4401/ag-7229.

Bonini, L. *et al.*, 2019. Testing different tectonic models for the source of the M_w 6.5, 30 October 2016, Norcia earthquake (central Italy): a youthful normal fault, or negative inversion of an old thrust? *Tectonics,* **38**(3), 990–1017.

Candela, T., Renard, F., Klinger, Y., Mair, K., Schmittbuhl, J. & Brodsky, E.E., 2012. Roughness of fault surfaces over nine decades of length scales, *J. geophys. Res.,* **117**(B8), B08409, doi:10.1029/2011JB009041.

Cheloni, D. *et al.*, 2014. Coseismic and post-seismic slip of the 2009 L'Aquila (central Italy) M_w 6.3 earthquake and implications for seismic potential along the Campotosto fault from joint inversion of high-precision levelling, InSAR and GPS data, *Tectonophysics,* **622,** 168–185.

Cheloni, D. *et al.*, 2016. GPS observations of coseismic deformation following the 2016, August 24, M_w 6 Amatrice earthquake (central Italy): data, analysis and preliminary fault model, *Ann. Geophys.,* **59,** doi:10.4401/ag-7269.

Cheloni, D. *et al.*, 2017. Geodetic model of the 2016 central Italy earthquake sequence inferred from insar and gps data, *Geophys. Res. Lett.,* **44**(13), 6778–6787.

Chiarabba, C., Bagh, S., Bianchi, I., De Gori, P. & Barchi, M., 2010. Deep structural heterogeneities and the tectonic evolution of the Abruzzi region

(central Apennines, Italy) revealed by microseismicity, seismic tomography, and teleseismic receiver functions, *Earth planet. Sci. Lett.,* **295**(34), 462–476.

Chiarabba, C., De Gori, P., Cattaneo, M., Spallarossa, D. & Segou, M., 2018. Faults geometry and the role of fluids in the 2016–2017 central Italy seismic sequence, *Geophys. Res. Lett.,* **45**(14), 6963–6971.

Chiaraluce, L., Barchi, M., Collettini, C., Mirabella, F. & Pucci, S., 2005. Connecting seismically active normal faults with Quaternary geological structures in a complex extensional environment: the Colfiorito 1997 case history (northern Apennines, Italy), *Tectonics,* **24**(1), doi:10.1029/2004TC001627.

Chiaraluce, L. *et al.*, 2017. The 2016 central Italy seismic sequence: a first look at the mainshocks, aftershocks, and source models, *Seismol. Res. Lett.,* **88**(3), 757–771.

D'Agostino, N., Cheloni, D., Fornaro, G., Giuliani, R. & Reale, D., 2012. Space-time distribution of afterslip following the 2009 L'Aquila earthquake, *J. geophys. Res.,* **117**(B2), B02402, doi:10.1029/2011JB008523.

Dettmer, J., Benavente, R., Cummins, P.R. & Sambridge, M., 2014. Transdimensional finite-fault inversion, *Geophys. J. Int.,* **199**(2), 735–751.

Dettmer, J., Hawkins, R., Cummins, P.R., Hossen, J., Sambridge, M., Hino, R. & Inazu, D., 2016. Tsunami source uncertainty estimation: the 2011 Japan tsunami, *J. geophys. Res.,* **121**(6), 4483–4505.

Diao, F., Wang, R., Aochi, H., Walter, T.R., Zhang, Y., Zheng, Y. & Xiong, X., 2016. Rapid kinematic finite-fault inversion for an M_w 7+ scenario earthquake in the Marmara Sea: an uncertainty study, *Geophys. J. Int.,* **204**(2), 813–824.

Di Stefano, R., Chiarabba, C., Chiaraluce, L., Cocco, M., De Gori, P., Piccinini, D. & Valoroso, L., 2011. Fault zone properties affecting the rupture evolution of the 2009 (M_w 6.1) L'Aquila earthquake (central Italy): insights from seismic tomography, *Geophys. Res. Lett.,* **38**(10), L10310, doi:10.1029/2011GL047365.

Duputel, Z., Rivera, L., Fukahata, Y. & Kanamori, H., 2012. Uncertainty estimations for seismic source inversions, *Geophys. J. Int.,* **190**(2), 1243–1256.

Duputel, Z., Agram, P.S., Simons, M., Minson, S.E. & Beck, J.L., 2014. Accounting for prediction uncertainty when inferring subsurface fault slip, *Geophys. J. Int.,* **197**(1), 464–482.

Duputel, Z. *et al.*, 2015. The Iquique earthquake sequence of April 2014: Bayesian modeling accounting for prediction uncertainty, *Geophys. Res. Lett.,* **42**(19), 7949–7957.

Elliott, J.R., Jolivet, R., Gonzlez, P.J., Avouac, J.-P., Hollingsworth, J., Searle, M.P. & Stevens, V.L., 2016. Himalayan megathrust geometry and relation to topography revealed by the Gorkha earthquake, *Nat. Geosci.,* **9**(2), 174–180.

EMERGEO Working Group, 2016a. The 24 August 2016 Amatrice earthquake: coseismic effects, *Tech. Rep.,* doi:10.5281/zenodo.61568.

EMERGEO Working Group, 2016b. Summary report on the 30 October, 2016 earthquake in central Italy M_w 6.5, *Tech. Rep.,* doi:10.5281/zenodo.166238.

Fukahata, Y. & Wright, T.J., 2008. A non-linear geodetic data inversion using ABIC for slip distribution on a fault with an unknown dip angle, *Geophys. J. Int.,* **173**(2), 353–364.

Fukuda, J. & Johnson, K.M., 2010. Mixed linear non-linear inversion of crustal deformation data: Bayesian inference of model, weighting and regularization parameters, *Geophys. J. Int.,* **181**(3), 1441–1458.

Gallovic, F., Imperatori, W. & Mai, P.M., 2015. Effects of three-dimensional crustal structure and smoothing constraint on earthquake slip inversions: case study of the M_w 6.3 2009 L'Aquila earthquake, *J. geophys. Res.,* **120**(1), 428–449.

Graymer, R.W., Langenheim, V.E., Simpson, R.W., Jachens, R.C. & Ponce, D.A., 2007. Relatively simple through-going fault planes at large-earthquake depth may be concealed by the surface complexity of strike-slip faults, *Geol. Soc. Lond. Spec. Publ.,* **290**(1), 189–201.

Hallo, M. & Gallovic, F., 2016. Fast and cheap approximation of Green function uncertainty for waveform-based earthquake source inversions, *Geophys. J. Int.,* **207**(2), 1012–1029.

Hartzell, S., Liu, P., Mendoza, C., Ji, C. & Larson, K.M., 2007. Stability and uncertainty of finite-fault slip inversions: application to the 2004 Parkfield, California, earthquake, *Bull. seism. Soc. Am.,* **97**(6), 1911–1934.

Herrmann, R.B., Malagnini, L. & Munafo, I., 2011. Regional moment tensors of the 2009 L'Aquila earthquake sequence, *Bull. seism. Soc. Am.,* **101**(3), 975–993.

Huang, M.-H., Fielding, E.J., Dickinson, H., Sun, J., Gonzalez-Ortega, J.A., Freed, A.M. & Burgmann, R., 2017a. Fault geometry inversion and slip distribution of the 2010 M_w 7.2 El Mayor-Cucapah earthquake from geodetic data, *J. geophys. Res.,* **122**(1), 607–621.

Huang, M.-H., Fielding, E.J., Liang, C., Milillo, P., Bekaert, D., Dreger, D. & Salzer, J., 2017b. Coseismic deformation and triggered landslides of the 2016 M_w 6.2 Amatrice earthquake in Italy, *Geophys. Res. Lett.,* **44**(3), 1266–1274 .

INGV Working Group (GPS data and data analysis center), 2016. *Preliminary co-seismic displacements for the August 24, 2016 ML6, Amatrice (central Italy) earthquake from the analysis of continuous GPS stations,* doi:10.5281/zenodo.61355.

Jiang, J. & Simons, M., 2016. Probabilistic imaging of tsunamigenic seafloor deformation during the 2011 Tohoku-Oki earthquake, *J. geophys. Res.,* **121**(12), 9050–9076.

Jolivet, R. *et al.*, 2012. Shallow creep on the Haiyuan Fault (Gansu, China) revealed by SAR Interferometry, *J. geophys. Res.,* **117**(B6), B06401, doi:10.1029/2011JB008732.

Jolivet, R., Simons, M., Agram, P.S., Duputel, Z. & Shen, Z.-K., 2015. Aseismic slip and seismogenic coupling along the central San Andreas Fault, *Geophys. Res. Lett.,* **42**(2), 297–306.

Lavecchia, G., Ferrarini, F., Brozzetti, F., Nardis, R.D., Boncio, P. & Chiaraluce, L., 2012. From surface geology to aftershock analysis: constraints on the geometry of the L'Aquila 2009 seismogenic fault system, *Ital. J. Geosci.,* **131**(3), 330–347.

Lavecchia, G. *et al.*, 2016. Ground deformation and source geometry of the 24 August 2016 Amatrice earthquake (central Italy) investigated through analytical and numerical modeling of DInSAR measurements and structural-geological data, *Geophys. Res. Lett.,* **43**(24), 12 389–12 398.

Lavecchia, G. *et al.*, 2017. Multidisciplinary inferences on a newly recognized active east-dipping extensional system in central Italy, *Terra Nova,* **29**(1), 77–89.

Lay, T., 2018. A review of the rupture characteristics of the 2011 Tohoku-Oki M_w 9.1 earthquake, *Tectonophysics,* **733,** 4–36.

Liu, C., Zheng, Y., Xie, Z. & Xiong, X., 2017. Rupture features of the 2016 M_w 6.2 Norcia earthquake and its possible relationship with strong seismic hazards, *Geophys. Res. Lett.,* **44**(3), 1320–1328.

Lohman, R.B. & Simons, M., 2005. Some thoughts on the use of InSAR data to constrain models of surface deformation: noise structure and data downsampling, *Geochem. Geophys. Geosyst.,* **6**(1), Q01007, doi:10.1029/2004GC000841.

Magnoni, F., Casarotti, E., Michelini, A., Piersanti, A., Komatitsch, D., Peter, D. & Tromp, J., 2014. Spectral element simulations of seismic waves generated by the 2009 L'Aquila earthquake, *Bull. seism. Soc. Am.,* **104**(1), 73–94.

Manighetti, I., Caulet, C., De Barros, L., Perrin, C., Cappa, F. & Gaudemer, Y., 2015. Generic along-strike segmentation of Afar normal faults, East Africa: implications on fault growth and stress heterogeneity on seismogenic fault planes, *Geochem. Geophys. Geosyst.,* **16**(2), 443–467.

Marchandon, M., Vergnolle, M., Sudhaus, H. & Cavalie, O., 2018. Fault geometry and slip distribution at depth of the 1997 M_w 7.2 Zirkuh earthquake: contribution of near-field displacement data, *J. geophys. Res.,* **123**(2), 1904–1924.

Michele, M. *et al.*, 2016. The Amatrice 2016 seismic sequence: a preliminary look at the mainshock and aftershocks distribution, *Ann. Geophys.,* **59,** doi:10.4401/ag-7227.

Minson, S.E., Simons, M. & Beck, J.L., 2013. Bayesian inversion for finite fault earthquake source models I: theory and algorithm, *Geophys. J. Int.,* **194**(3), 1701–1726.

Minson, S.E. *et al.*, 2014. Bayesian inversion for finite fault earthquake source models II: the 2011 great Tohoku-Oki, Japan earthquake, *Geophys. J. Int.,* **198**(2), 922–940.

Okubo, P.G. & Aki, K., 1987. Fractal geometry in the San Andreas Fault system, *J. geophys. Res.,* **92**(B1), 345–355.
Parzen, E., 1962. On estimation of a probability density function and mode, *Ann. Math. Stat.,* **33**(3), 1065–1076.
Peacock, D. C.P., 1991. Displacements and segment linkage in strike-slip fault zones, *J. Struct. Geol.,* **13**(9), 1025–1035.
Pizzi, A. & Galadini, F., 2009. Pre-existing cross-structures and active fault segmentation in the northern-central Apennines (Italy), *Tectonophysics,* **476**(1), 304–319.
Pizzi, A., Di Domenica, A., Gallovic, F., Luzi, L. & Puglia, R., 2017. Fault segmentation as constraint to the occurrence of the main shocks of the 2016 central Italy seismic sequence, *Tectonics,* **36**(11), 2370–2387.
Power, W.L., Tullis, T.E., Brown, S.R., Boitnott, G.N. & Scholz, C.H., 1987. Roughness of natural fault surfaces, *Geophys. Res. Lett.,* **14**(1), 29–32.
Pucci, S. *et al.*, 2017. Coseismic ruptures of the 24 August 2016, M_w 6.0 Amatrice earthquake (central Italy), *Geophys. Res. Lett.,* **44**(5), 2138–2147.
Ragon, T., Sladen, A. & Simons, M., 2018. Accounting for uncertain fault geometry in earthquake source inversions I: theory and simplified application, *Geophys. J. Int.,* **214**(2), 1174–1190.
Razafindrakoto, H.N.T. & Mai, P.M., 2014. Uncertainty in earthquake source imaging due to variations in source time function and earth structure, *Bull. seism. Soc. Am.,* **104**(2), 855–874.
Ross, Z.E., Hauksson, E. & Ben-Zion, Y., 2017. Abundant off-fault seismicity and orthogonal structures in the San Jacinto fault zone, *Sci. Adv.,* **3**(3), e1601946, doi:10.1126/sciadv.1601946.
Segall, P. & Pollard, D.D., 1980. Mechanics of discontinuous faults, *J. geophys. Res.,* **85**(B8), 4337–4350.
Simons, M., Fialko, Y. & Rivera, L., 2002. Coseismic deformation from the 1999 M_w 7.1 Hector Mine, California, earthquake as inferred from InSAR and GPS observations, *Bull. seism. Soc. Am.,* **92**(4), 1390–1402.
Sun, J., Johnson, K.M., Cao, Z., Shen, Z., Burgmann, R. & Xu, X., 2011. Mechanical constraints on inversion of coseismic geodetic data for fault slip and geometry: example from InSAR observation of the 6 October 2008 M_w 6.3 DangxiongYangyi (Tibet) earthquake, *J. geophys. Res.,* **116**(B1), B01406.
Tarantola, A., 2005. *Inverse Problem Theory and Methods for Model Parameter Estimation,* Society for Industrial and Applied Mathematics.
Tinti, E., Scognamiglio, L., Michelini, A. & Cocco, M., 2016. Slip heterogeneity and directivity of the ML 6.0, 2016, Amatrice earthquake estimated with rapid finite-fault inversion, *Geophys. Res. Lett.,* **43**(20), 10 745–10 752.
Trasatti, E., Kyriakopoulos, C. & Chini, M., 2011. Finite element inversion of DInSAR data from the M_w 6.3 L'Aquila earthquake, 2009 (Italy), *Geophys. Res. Lett.,* **38**(8), L08306, doi:10.1029/2011GL046714.
Tung, S. & Masterlark, T., 2018. Resolving source geometry of the 24 August 2016 Amatrice, central Italy, earthquake from InSAR data and 3D finite element modeling, *Bull. seism. Soc. Am.,* **108**(2), 553–572.
Walsh, J.J., Bailey, W.R., Childs, C., Nicol, A. & Bonson, C.G., 2003. Formation of segmented normal faults: a 3-D perspective, *J. Struct. Geol.,* **25**(8), 1251–1262.
Wang, K. & Fialko, Y., 2015. Slip model of the 2015 M_w 7.8 Gorkha (Nepal) earthquake from inversions of ALOS-2 and GPS data, *Geophys. Res. Lett.,* **42**(18), 7452–7458.
Wei, S. *et al.*, 2011. Superficial simplicity of the 2010 El Mayor-Cucapah earthquake of Baja California in Mexico, *Nat. Geosci.,* **4**(9), 615–618.
Yagi, Y. & Fukahata, Y., 2011. Introduction of uncertainty of Green's function into waveform inversion for seismic source processes, *Geophys. J. Int.,* **186**(2), 711–720.
Yue, H. *et al.*, 2017. Depth varying rupture properties during the 2015 M_w 7.8 Gorkha (Nepal) earthquake, *Tectonophysics,* **714,** 44–54.
Zhu, L. & Rivera, L.A., 2002. A note on the dynamic and static displacements from a point source in multilayered media, *Geophys. J. Int.,* **148**(3), 619–627.

SUPPORTING INFORMATION

Supplementary data are available at *GJI* online.

Table S1. Interferometric pairs used in this study.
Table S2. Residuals between observations and predictions (RMS in centimetre) for models inferred assuming fault geometries A and B, accounting or not for C_p.
Table S3. Residuals (RMS in centimetre) for the synthetic inversion with the first target model, assuming a wrong dip of 10° and an incorrect crustal structure, accounting or not for C_p in fault geometry or/and crustal structure.
Figure S1. Assumed elastic properties of the Earth and their associated uncertainties. V_s is illustrated with a red line, V_p with a dashed red line, V_p with a dotted red line and their values are detailed in the bottom axis. μ is illustrated by a blue line and legended in the top of the figure. The uncertainties associated with each parameter are also illustrated. The distribution of elastic parameters are log-normal because the elastic parameters are Jeffrey's parameters (Tarantola 2005; Duputel *et al.* 2014). λ is estimated from V_p ,V_s, ρ and μ and thus its distribution derives from the distribution of these parameters.
Figure S2. Empirical covariance functions for the ALOS 2 descending interferogram. Radially symmetric empirical covariance functions and associated best-fitting exponential functions for the displacements derived from InSAR data. For each interferogram, we compute the empirical covariance as a function of the interpixel distance and then fit an exponential function (Jolivet *et al.* 2012). The exponential function is used to build the data covariance matrix.
Figure S3. The set of samples inferred from an inversion is divided into 25 subsets. The first family gathers samples whose parameters are of less than 50 cm offset from the median model parameters. In detail, a model is added to the first family if the selected model and the median model are parameter-wise equal within a relative tolerance of 20 per cent added to an absolute tolerance of 50 cm for the co-seismic slip, and a relative tolerance of 10 per cent added to an absolute tolerance of 25 cm for the post-seismic slip. Other families are built iteratively around a randomly selected model that has not fitted within antecedent families, except for the last family that regroups orphan samples. In (a), one model of each subset inferred without accounting for C_p and assuming fault geometry A is selected randomly. In (b), the median model of each of the 25 subsets is shown. In the main text, Figs 2(c) and (d), 4(a)–(h), 5(a) and (b) and 6(c) and (d) derive from the combination of random models—as in (a)—while Figs 10(a)–(f) are obtained from the combination of median models—as in (b).
Figure S4. Comparison between posterior marginal PDFs of the dip-slip parameters inferred with fault geometry A and B. Parameters inferred assuming fault geometry A are in the foreground. In the last four rows, the PDFs show the repartition of parameters for patches covering two subfaults along strike and two subfaults along dip (i.e. patches two times bigger than for the first four rows). The offset between the median models is shown as percentage with a different colour scale.
Figure S5. Fit of the InSAR Sentinel data set for an inversion made assuming fault geometry B and no C_p. Observations, predictions inferred from the average model and residuals are shown for Sentinel 1 ascending and descending interferograms, respectively, to the left and to the right. The assumed fault trace is shown with a dark grey line. Seismogenic faults are shown in light grey.
Figure S6. Fit of the InSAR ALOS data set for an inversion made assuming fault geometry B and no C_p. Observations, predictions inferred from the average model and residuals are shown for ALOS

2 ascending and descending interferograms, respectively, to the left and to the right. The assumed fault trace is shown with a dark grey line. Seismogenic faults are shown in light grey.

Figure S7. Fit of the InSAR Sentinel data set for an inversion made assuming fault geometry A and no C_p. Observations, predictions inferred from the average model and residuals are shown for Sentinel 1 ascending and descending interferograms, respectively, to the left and to the right. The assumed fault trace is shown with a dark grey line. Seismogenic faults are shown in light grey.

Figure S8. Fit of the InSAR ALOS data set for an inversion made assuming fault geometry A and no C_p. Observations, predictions inferred from the average model and residuals are shown for ALOS 2 ascending and descending interferograms, respectively, to the left and to the right. The assumed fault trace is shown with a dark grey line. Seismogenic faults are shown in light grey.

Figure S9. Comparison of three finite-fault slip models inferred from the target model illustrated in Fig. 4(a), assuming an incorrect fault dip of 10. (with the position of fault A) and an incorrect elastic structure. In (a), we do not assume any uncertainties. In (b), we account for C_p^{fault} and in (c) for $C_p^{fault+earth}$. Each figure illustrates the posterior marginal PDFs of the inferred models, and the target slip model is delineated with a red line.

Figure S10. Comparison between posterior marginal PDFs of the dip-slip parameters inferred with fault geometry A and B, accounting for C_p in fault geometry. Parameters inferred assuming fault geometry A are in the foreground. In the last four rows, the PDFs show the repartition of parameters for patches covering two subfaults along strike and two subfaults along dip (i.e. patches two times bigger than for the first four rows). The offset between the median models is shown as percentage with a different colour scale.

Figure S11. Comparison of the residuals between inversion accounting or not for C_p and with fault geometry A as reference. The residuals corresponding to dip-slip amplitudes of average models are presented in terms of percentage of slip (left) or as absolute values (right).

Figure S12. Fit of the InSAR Sentinel data set for an inversion made assuming fault geometry A and accounting for C_p. Observations, predictions inferred from the average model and residuals are shown for Sentinel 1 ascending and descending interferograms, respectively, to the left and to the right. The assumed fault trace is shown with a dark grey line. Seismogenic faults are shown in light grey.

Figure S13. Fit of the InSAR ALOS data set for an inversion made assuming fault geometry A and accounting for C_p. Observations, predictions inferred from the average model and residuals are shown for ALOS 2 ascending and descending interferograms, respectively, to the left and to the right. The assumed fault trace is shown with a dark grey line. Seismogenic faults are shown in light grey.

Figure S14. Comparison of two finite-fault slip models inferred accounting for C_p in fault geometry (left) or for C_p in both fault geometry and crustal structure (right). (a) and (b) show the slip amplitude and rake of the average model, the epicentre being the white star. The colour scale is valid for all the figures. (c) and (d) illustrate the slip amplitude of 25 random samples chosen among the most probable models. Each subfault (the large square) thus contains 25 pixels coloured according to the slip amplitude of the corresponding random sample. (e) and (f) represent the posterior marginal PDFs. 15

Figure S15. The deep high-slip area is recquired to explain some features of the InSAR data. Model (1) corresponds to the average model estimated assuming geometry A and without C_p, but with zero slip below 7 km depth. In contrast, Model (2) has subfaults slipping of 75 cm below 7 km depth, at the location of the deep high-slip area, and no slip in other subfaults. (a), (c) and (e) show the residuals between the interferograms and the predictions of Model (1). (b) (d) and (f) show the predictions of Model (2) for the same interferograms and colour-scale as in (a), (c) and (e). The red circle delineates the area with the largest predicted surface deformation using Model (2)—as in (b), (d) and (f)—which corresponds to a deficit of surface deformation in the residuals plotted in (a), (c) and (e).

Figure S16. Comparison of finite-fault slip models inferred accounting for different C_p matrices (b–f) or not (a). Figures illustrate the posterior marginal PDFs for the four first rows and the mean of the posterior marginal PDFs over two subfaults along dip and two subfaults along strike for the four last rows (i.e. the PDFs for doubled-size subfaults). (a) No C_p is accounted for (same model as in Fig. 2a). (b) Only C_p^{dip} is included, and the matrix has been computed with a prior standard deviation of 2.5°. (c) Only C_p^{earth} is introduced. (d) Only C_p^{fault} is accounted for (same model as in Fig. 6a). (e) Both C_p^{fault} and C_p^{earth} are accounted for (same model as in Supporting Information Fig. S14b). (f) Both C_p^{fault} and C_p^{earth} are accounted for such that $C_p = 2 \times (C_p^{fault} + C_p^{earth})$.